Fuel 336 (2023) 126806

Contents lists available at ScienceDirect

Fuel

journal homepage: www.elsevier.com/locate/fuel

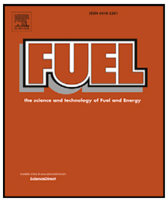

Deep learning for characterizing CO_2 migration in time-lapse seismic images

Hanlin Sheng [a,b], Xinming Wu [a,b,*], Xiaoming Sun [a,b], Long Wu [c]

[a] *Laboratory of Seismology and Physics of Earth's Interior, School of Earth and Space Sciences, University of Science and Technology of China, No. 96, JinZhai Road Baohe District, Hefei, 230026, Anhui, PR China*
[b] *Mengcheng National Geophysical Observatory, University of Science and Technology of China, Hefei, 230026, Anhui, PR China*
[c] *Equinor ASA, Sandsliveien 90, 5254, Bergen, Norway*

ARTICLE INFO

Keywords:
Seismic data
Seismic interpretation
Deep learning
CO_2 characterization
Convolutional neural network
CO_2 migration

ABSTRACT

Time-lapse (or 4-D) seismic data play an important role in monitoring the spatial CO_2 distribution during and after the injection period. However, traditional interpretation or prediction of CO_2 distribution is time-consuming and might be sensitive to the quality of 4D seismic data. To solve these problems, we propose a deep-learning-based method to efficiently and accurately characterize CO_2 plumes in time-lapse seismic data. We first introduce a workflow to build 3-D realistic impedance models containing CO_2 plumes with various shapes, sizes, and locations. From the impedance models, we then simulate synthetic seismic datasets and automatically obtain the corresponding CO_2 label volumes. We extract real noise from field seismic datasets and add the noise to the synthetic ones to make them more realistic. We further construct a diverse and realistic training dataset with the combination of synthetic data containing CO_2 plumes and real data without CO_2 plumes that are randomly cropped from field seismic data before CO_2 injection. We finally utilize the training datasets without any human labeling to train a 3-D deep U-shape convolutional neural network for detecting CO_2 plumes in the Sleipner time-lapse seismic images. Compared to traditional interpretation methods that take several days or even weeks, our method takes only 29 s using one graphics processing unit (GPU) to predict CO_2 plumes in a 512*512*256 seismic volume. Besides, our CO_2 prediction can achieve 95.8% accuracy (compared to the manual interpretation) and could distinguish reflections of CO_2 plumes from the ones of pre-existing fluids, thin layers, and noise. To more accurately characterize the CO_2 plumes migration, we use dynamic image warping to compute relative shifts that register the time-lapse seismic volumes before and after CO_2 injection and then apply the same shifts to the predicted CO_2 plumes. By doing this, we are able to reduce the inconsistencies that may be introduced by acquisition, processing, push-down effect (velocity decrease by injected CO_2), and pull-up effect (wavelet distortion), which is helpful to more accurately characterize the CO_2 plumes migration.

1. Introduction

Carbon Capture, Utilization and Storage (CCUS) is one important approach to solve global climate change. CCS aims to separate CO_2 from emission sources or air [1–3], transport the collected CO_2 to storage sites, and isolate CO_2 from the atmosphere. The Geological CO_2 Sequestration (GCS) has been proven to be one effective CCS method according to several successful CO_2 injection projects: the Sleipner project in Norway, the Weyburn EOR project in Canada, and the In Salah project in a gas field in Algeria [4–6]. The Sleipner CO_2 injection project is the world's first industrial offshore CO_2 CCS project. Since September 15, 1996, CO_2 has been injected into the Utsira Formation aquifer close to the Sleipner Øst platform. The injection rate is at approximately 0.9 Mt for the first year through injection well 15/9-A-16, and has been decreasing slightly each year since then [7–11]. By 2020, around 18.5 million tonnes of CO_2 have been stored underground [12].

Injecting CO_2 into the subsurface would be at risk of leakage, so monitoring the CO_2 migration is crucial. In the Sleipner area, a number of methods are used to monitor CO_2 migration, including well logging, time-lapse seismic surveys [13,14], gravity [15–17], and Controlled Source Electromagnetic [18,19]. Well logging, as the most direct method to observe the subsurface, provides the most accurate geologic formations. However, well logging is costly and increases the potential risk of CO_2 leakage. Therefore, only one CCS monitoring well

---

[*] Corresponding author at: Laboratory of Seismology and Physics of Earth's Interior, School of Earth and Space Sciences, University of Science and Technology of China, No. 96, JinZhai Road Baohe District, Hefei, 230026, Anhui, PR China.
E-mail address: xinmwu@ustc.edu.cn (X. Wu).

https://doi.org/10.1016/j.fuel.2022.126806
Received 27 July 2022; Received in revised form 16 October 2022; Accepted 14 November 2022

(16/7-3) is explored in the Sleipner which is not sufficient to most studies [7]. The Controlled Source Electromagnetic (CSEM) method can also be useful for monitoring CO_2 migration [18,19]. Due to the lack of time-lapse data and limited resolution, it is difficult to depict the CO_2 migration process exactly through CSEM. Gravity surveys can provide the measurement of density changes, that might be related to CO_2 saturation. However, the gravity anomalies caused by the pure CO_2 response might be affected by irrelevant factors, like ocean tidal fluctuations, scouring by sea-bottom currents, and so on [11]. These interference factors cannot be easily separated from the gravity anomalies, which requires processing the gravity data with considerable time and efforts.

A time-lapse seismic survey serves an important role in characterizing CO_2 migration in the Sleipner field. The injected CO_2 replaces brine in the pore space of the rock, thus creating strong impedance contrasts. These contrasts generate obvious responses in the seismic data [20]. With these time-lapse seismic data, some scholars develop various methods on how to monitor the CO_2 migration in the subsurface. Quantitative seismic analysis is one of the key solutions to detect the CO_2 migration. This approach typically characterizes CO_2 plumes by analyzing anomalies amplitude, or the downward bending of the underlying layers (push-down) caused by CO_2-induced low-velocity [21–24]. Limited by the seismic data quality, the results of these methods may be affected by noise or other interferences, thus leading to some uncertainty in these methods. Another approach is to inverse the elastic impedance and velocity with different inversion methods like FWI [25], and stratigraphic inversion [26]. The inverted subsurface models are then used to analyze the CO_2 migration. However, the accuracy of the inversion results is highly dependent on initial models or the control of well logs which are typically missing in CCS projects. Besides, models based on fluid simulation are often used to detect CO_2 migration [12,27–33]. However, the initialization parameters related to the fluid simulation are abundant and dependent on the experience of interpreters.

Deep learning achieves many successful applications in the field of computer vision as well as in geoscience. The emergence of the Convolutional neural network (CNN) promotes the development of deep learning in various computer vision tasks. The applications of CNN for semantic segmentation [34–36], object detection [37–40], and instance segmentation [41–44] are very similar to geophysical problems. Many scholars demonstrate the reliability and efficiency of deep learning in many geophysical applications: geophysical imaging [45], inversion [46–48], and some subsurface typical features identification such as faults [49,50], salt-body delineation [51,52], paleokarst collapse [53], horizons [54,55], channels [56,57], fluid reservoirs [58,59].

Deep learning-based CO_2 identification has also achieved many successful cases in recent years. Many geophysicists utilize different deep-learning-based methods to investigate the relationship between permeability, porosity, and phase saturations, and further predict the CO_2 migration or the potential CO_2 leakage risk [60–63]. Meanwhile, some geophysicists develop deep-learning-based methods that can characterize CO_2 migration in seismic data. Li et al. [64] utilize the velocity decreasing anomalies to represent CO_2 in the P-wave velocity model. With the velocity models before and after CO_2 injection, they simulate two corresponding shot gathers and further calculate their difference as the input for the fully convolutional neural network (FCN). However, the difference in field data is not pure CO_2 responses which can be affected by amplitude difference, noise, and phase shift. Li and Li [65] input field seismic images before and after CO_2 injection to map the manual interpretation of CO_2 label volumes. Indeed, manually labeled data will guide the network to extract more accurate features and precise prediction results. However, manually labeled data is time-consuming and heavily dependent on expert judgments. In addition, the number and diversity of the manually labeled datasets may not be necessarily enough to train a network. Moreover, the model trained by labels from one survey might not be able to apply to other surveys.

We propose a fully automatic workflow without any human interaction for CO_2 characterization in time-lapse images and take the Sleipner as an example to demonstrate the workflow. In this paper, we first briefly introduce the geologic background of the Sleipner field survey. We then prepare the datasets used to train the neural network, including both synthetic and field data. In training datasets preparation, we first include baseline seismic data with empty CO_2 label volumes into the training datasets to prevent the network from making wrong predictions of the seismic reflection features that are similar to but not related to the CO_2 plumes. We then introduce a workflow to automatically simulate synthetic seismic datasets from randomly generated impedance models based on geophysical statistical data. We then include diffusive CO_2 plumes with various impedance patterns, shapes, and sizes into the impedance models. After obtaining the impedance model in the depth domain, we further utilize depth-time conversion to transform it into the time domain, which keeps our training data and the field data in the same domain. We further add folding structures and real noise extracted from field seismic images into the synthetic seismic images to make them more realistic. In this way, we are able to obtain diverse seismic data and the corresponding CO_2 label volumes for training the network. After training datasets preparation, we then present a 3-D convolutional neural network based on the U-net architecture and train it with both synthetic and field datasets to predict CO_2 plumes in 3-D field seismic images. With the whole datasets without any human labeling, the network can make a robust and accurate prediction of CO_2 plumes in the Sleipner seismic images acquired at different years. From the predicted CO_2 probability volumes, we can further extract the 3-D bodies of CO_2 plumes for quantitative analysis of the CO_2 migration through time. In order to obtain more accurate CO_2 migration through time, we further register all the time-lapse seismic volumes to the registered baseline seismic volume. By doing this, we are able to eliminate the time shifts of the CO_2 plumes that are not related to their migration but resulted from the push-down effects due to the velocity variation during the CO_2 injection and the pull-up effect due to wavelet distortion.

2. Geologic background and datasets of the Sleipner survey

Sleipner is located in Norway (the lower-left inset map in Fig. 1a) and has been evaluated by many geological and geophysical experts as a suitable CO_2 injection field. CO_2 should be typically stored in reservoirs more than 800 m deep underground, where the temperature varies between 35 degree and 40 degree and the pressure varies between 8 (MPa) and 10 (MPa) in Sleipner. These surrounding pressure and temperature conditions can keep CO_2 in a liquid or supercritical state [66]. Under these conditions, the density of CO_2 is 50 to 80 percent of the density of brine, where the buoyancy can drive the CO_2 to migrate upwards as shown by the arrows in Fig. 1a. Therefore, a storage site with good sealing capability is important to ensure that CO_2 is confined to the subsurface. The Sleipner field provides a good CO_2 storage site. The target layer of the CO_2 injection is the Mio-Pliocene layer Utsira Formation [67]. The top surface of the Utsira sand varies very smoothly over a depth range of 550–1500 m. The bottom structure of the Utsira sand is more complex and is characterized as mud bottom incipient [68]. Inside the sandstone body, many thin intra-reservoir (typically <1 m thick) shales are deposited, which separate spatially discontinuous layers in the interior of the Utsira sand. However, these thin shales cannot be easily correlated between wells and are not observable on the seismic data acquired prior to CO_2 injection [22]. As shown in the seismic data acquired before CO_2 injection in 1994 (Fig. 1b) and after CO_2 injection in 2006 (Fig. 1c), the intra-reservoir shales begin to become visible after CO_2 injection. Based on the wells and seismic data with CO_2 injection, many experts interpret the layers in the Utsira Sand Fm black lines in Fig. 1b and c.

The Utsira sand is separated from the upper 26 m thick Pliocene sand wedge (i.e., Top sand Wedge) by an approximately 6 m thick

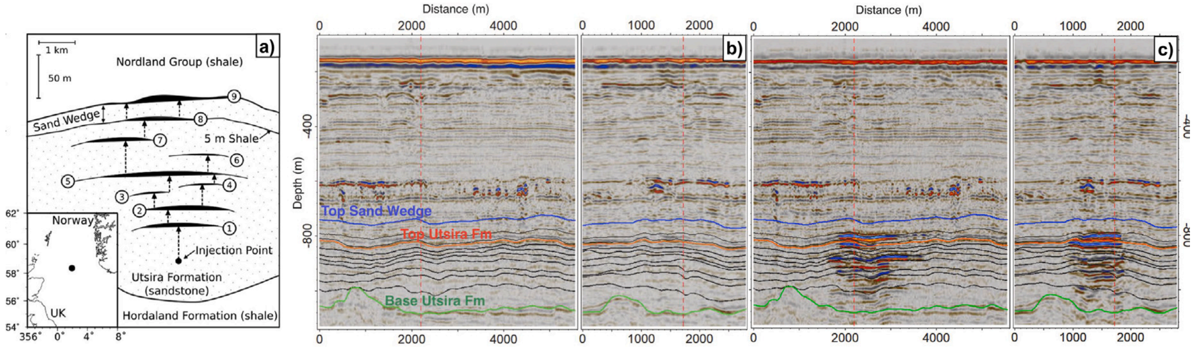

Fig. 1. (a) The schematic diagram of nine CO_2 filled layers and the inset map (lower-left) shows the general location of the Sleipner project. The arrows represent the schematic diagram of the rising CO_2 plumes (modified after [70]). The crossline (left) and inline (right) sections of the Sleipner time-lapse seismic data with and without CO_2 injection are shown in (b) and (c), respectively. The interpreted layers results of Utsira Sand Fm and Top sand Wedge are more clearly to visualize only when CO_2 is injected as shown in (c) (modified after [71]).

Table 1
The years of acquisition and processing for available seismic images in the 4-D Sleipner seismic dataset.

Processed year	Acquired data
2001	1994,1999,2001
2007	1994,2001,2004,2006
2008	1994,2008
2010	1994,2010
2011	2010

shale layer. Both Utsira and Top Sand Wedge have high porosity (35%–40%), high net/gross (98%), and 1 to 5 Darcy permeabilities [68]. Above these good reservoirs is an overlying Nordland Gp shale with a thickness of more than 250 m, and the thick caprock provides relatively good confining conditions for the reservoirs [11].

The Sleipner 4D Seismic Dataset is a reference dataset from the Sleipner CO_2 storage site, which is made accessible to the public by Equinor [69]. The baseline data is acquired in 1994 before CO_2 injection. Subsequently, starting in 1996, CO_2 is continuously injected into the subsurface every year. By the year 2021, 18.5 Mt of CO_2 has been injected into the storage. Along with the CO_2 injection, several seismic surveys have been carried out to ensure that we can access the CO_2 migration including in 1999, 2001, 2002, 2004, 2006, 2008, 2010, 2012, and 2016 [69]. Since the acquisition and processing are not done simultaneously, the data was formed into multiple data pairs with baseline data for the year 1994 (Table 1). To facilitate the description, we simplify the year of acquisition and processing into a formulaic expression, such as $xx\mathbf{p}yy$. xx represents the year of acquisition and yy represents the year of processing. For example, $01\mathbf{p}07$ represents the data acquired in 2001 and processed in 2007. Every data in this provided datasets contains four stacked types including near-, medium-, far- and all-stacks. We take the nea-stacks data as the input data which are adequate for the CO_2 interpretation in this study [65]. We consider the characterization of CO_2 plumes in these time-lapse seismic images as a binary image segmentation problem and propose a 3-D convolutional neural network to solve this problem.

3. Training datasets preparation

As a data-driven approach, the deep neural network typically requires a lot of training datasets for optimizing its model parameters. In this section, we introduce the whole workflow for preparing the training datasets. The datasets consist of two subsets including field datasets and synthetic datasets. The field datasets contain a set of field seismic volumes with empty CO_2 plumes that are randomly cropped from the field baseline data without CO_2 injection. Therefore, the CO_2 label volumes within field datasets are filled with all zeros. The synthetic datasets contain abundant and diverse synthetic seismic data using stochastic simulation and seismic forward modeling. Therefore, the CO_2 label volumes within synthetic datasets are accurate. With both the field datasets and synthetic datasets, we are able to obtain a large amount of training datasets for training the neural network.

3.1. Field training datasets

Before injecting CO_2 into the subsurface at a storage site, we often firstly need to assess the storage capacity and containment risks of the CO_2 storage site by acquiring seismic data, which is also called baseline data. The baseline data can be taken as a reference to compare with the seismic datasets after CO_2 injection to estimate the distribution of CO_2. Based on this consideration, we show the seismic data before CO_2 injection in 1994 (Fig. 2a) and after CO_2 injection in 2010 (Fig. 2b) to indicate the CO_2 responses in seismic data. The green box indicates the approximate location of CO_2 plumes in $10\mathbf{p}10$ (Fig. 2b). The reflectors within the green box become more distinctive after CO_2 injection. As discussed above, CO_2 replaces brine thus creating strong impedance contrasts and further producing a high magnitude of amplitude in seismic data. However, the high magnitude of amplitude does not necessarily correspond to the existence of CO_2 as denoted by the red arrows in Fig. 2. Fortunately, we can identify these features as non-CO_2 features by comparing baseline seismic data before CO_2 injection in Fig. 2a. Inspired by this comparison approach, we randomly crop some sub-volumes of the field baseline data before CO_2 injection and include them in the whole training datasets. The participation of these baseline field data in the neural network training not only keeps the network away from incorrectly identifying some non-CO_2 reflection features but also allows the network to recognize the structural information of the Sleipner area. This is helpful to improve the generalization of the trained neural network on the field seismic data. Such a strategy of jointly using both field datasets and synthetic datasets can be used for any CO_2 survey because we always have a baseline seismic volume without CO_2 inject in each survey.

The baseline data are acquired in 1994 and processed in four different years as shown in Table 1. To eliminate errors introduced in the processing, we randomly crop the $94\mathbf{p}01$, $94\mathbf{p}07$, $94\mathbf{p}08$, and $94\mathbf{p}10$ datasets to join the training datasets without CO_2 injection. We randomly extract 16 subsets of the baseline field seismic data before CO_2 injection and the corresponding CO_2 label volumes are zeros everywhere. In fact, feeding an excessive number of sample pairs with empty labels in network training may lead to instability. So here we prepare only 16 pairs of field datasets and feed them randomly into the training process. We will explain more details in the $Training\ and\ Validation$ part.

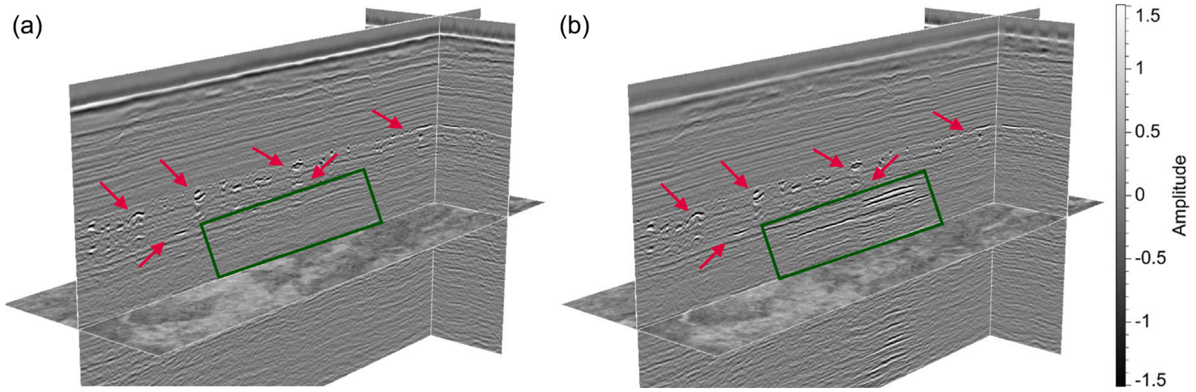

Fig. 2. The Sleipner time-lapse seismic data is acquired in 1994 (a) and 2010 (b). The layers after CO_2 injection show stronger seismic reflection (within the green boxes) than those before the CO_2 injection. Some other strong reflection features denoted by red arrows may be misidentified as CO_2 if the baseline data (a) without CO_2 injection is not available. (For interpretation of the references to color in this figure legend, the reader is referred to the web version of this article.)

3.2. Synthetic training datasets

Based on prior geological knowledge and geophysical laws, we propose a workflow (Fig. 3) to automatically generate synthetic datasets for training our deep neural network. We first synthesize a flat impedance model as an initial geological model (Fig. 3a), where the velocities follow the statistic distribution of Sleipner field velocities and the corresponding densities follow the Gardner relation [72]. We then simulate a diffusion coefficient map (Fig. 3b) by randomly choosing the locations of an injection point and a series of migration feeders for upward CO_2, where the locations of the injection point and migration feeders are within sandstone layers in the geological model. With the diffusion coefficient map based on the geological model, we further simulate CO_2 plumes by simply solving a diffusion equation to morphologically approximate the CO_2migration. We then modify the impedance values within the simulated CO_2 plumes (Fig. 3d) according to the physical equations for the decay of velocity and density with CO_2 saturation. After CO_2 injection, we transform the depth-domain impedance model into a time-domain impedance model (Fig. 3e) using depth-time conversion. We then compute the corresponding reflectivity model (Fig. 3f) and further convolve the reflectivity model with a wavelet to simulate seismic data (Fig. 3g). To make the synthetic seismic data more realistic, we implement some folding (Fig. 3h) and add real noise extracted from field data to obtain the final synthetic seismic image (Fig. 3i). Besides, we can apply the depth-time conversion to map the CO_2 plumes from the depth domain (Fig. 3c) to the time domain (Fig. 3q). Since we use the same velocity model for both the conversion of CO_2 plumes and impedance model used to simulate the seismic data, the labels of CO_2 plumes and the corresponding seismic data will be consistent in the time domain after the conversion. In this way, we are able to obtain synthetic training dataset pairs of a seismic volume and the corresponding CO_2 labels like the ones in Figures (Fig. 3i and j). In the following part, we will introduce each step of the synthetic data workflow in more detail.

3.2.1. Building an initial flat impedance model

We firstly simulate a stochastic impedance model, where the 3-D grid cell size is defined as 12.5 m × 12.5 m × 1 m in x, y, and z (depth) directions. The stochastic simulation on flat impedance models requires two parameters: the thickness of each layer and the corresponding impedance distribution. To make the synthetic data more realistic compared to the field data, we utilize statistical data from Equinor geological models to determine the layer thickness and impedance distribution. According to the geological models in the Sleipner survey [4], the interior of the CO_2-injected layers consists of sandstone with a thickness ranging from 30 to 116 m, interspersed with shales with a thickness ranging from 0.5 to 1.5 m. Equinor geological models also provide a human-picking velocity model on Utsira Sand Formation and Pliocene Sand Wedge. Fig. 3i shows the results of the velocity statistical histograms of the Utsira Sand Formation (green area) and Pliocene Sand Wedge (blue area) and the corresponding fitted Gaussian distribution curves. These two statistics can be considered as the distribution of velocities for the sandstone since the velocities of shale occupy only a tiny fraction of the statistics.

With all these statistical data, the sandstone layer thickness is randomly selected between 25 to 50 m, while the shale layer thickness is set to 1 m. After determining the thickness of each layer, we further determine the velocities of each layer based on statistical Gaussian distributions of sandstone and shale shown in Fig. 3k. In these distributions, the mean velocity value of each sandstone layer is randomly chosen from 2000 to 2250 (m/s). While the mean velocity value of each shale layer is randomly chosen from 2300 to 2400 (m/s). The ranges of mean velocities are determined by the statistical analysis of the well-log data near the survey [73]. The variances of each sandstone layer and each shale layer are both randomly chosen from 200 to 400 (m/s). The corresponding densities can be obtained through the Gardner relation with the determined velocity:

$$\rho = \alpha V_p^{\beta}, \tag{1}$$

where ρ is density given in g/cm^3, V_p is P-wave velocity, and α and β are empirically derived constants that depend on the geology. Gardner et al. [72] propose that the relationship can be a good fit by taking $\alpha = 0.23$ and $\beta = 0.25$. With the velocities and densities settled, we are able to automatically obtain a series of synthetic flat impedance models like the one in Fig. 3a where the sandstone and shale layers intersect each other.

3.2.2. Simulating CO_2 plumes

We secondly simulate CO_2 plumes by simply solving a diffusion equation to morphologically approximate the CO_2 migration. In order to obtain diffusive CO_2 plumes, we first define a 3-D map of diffusion coefficients ranging from 0 to 1 as shown in Fig. 3b. Such a coefficient map is calculated in accordance with the upward migration of CO_2 rule, where the diffusion coefficient within each sandstone layer is inversely proportional to the distance to the separating shale on the top of the sandstone layer. Besides, we set the diffusion coefficients within randomly selected injection points and CO_2 migration feeders to be relatively higher, which ensures that the CO_2 migrates from the source (injection point), following the feeder paths, to the top of each sandstone layer. In this way, the CO_2 trends to be concentrated at the top of sandstone layers and trapped by the upside shale layers. CO_2 then will migrate through the shale layers to upper sandstones through the feeder paths. After the diffusion coefficients are established, we also introduce some lateral variations and irregular ellipsoid areas into

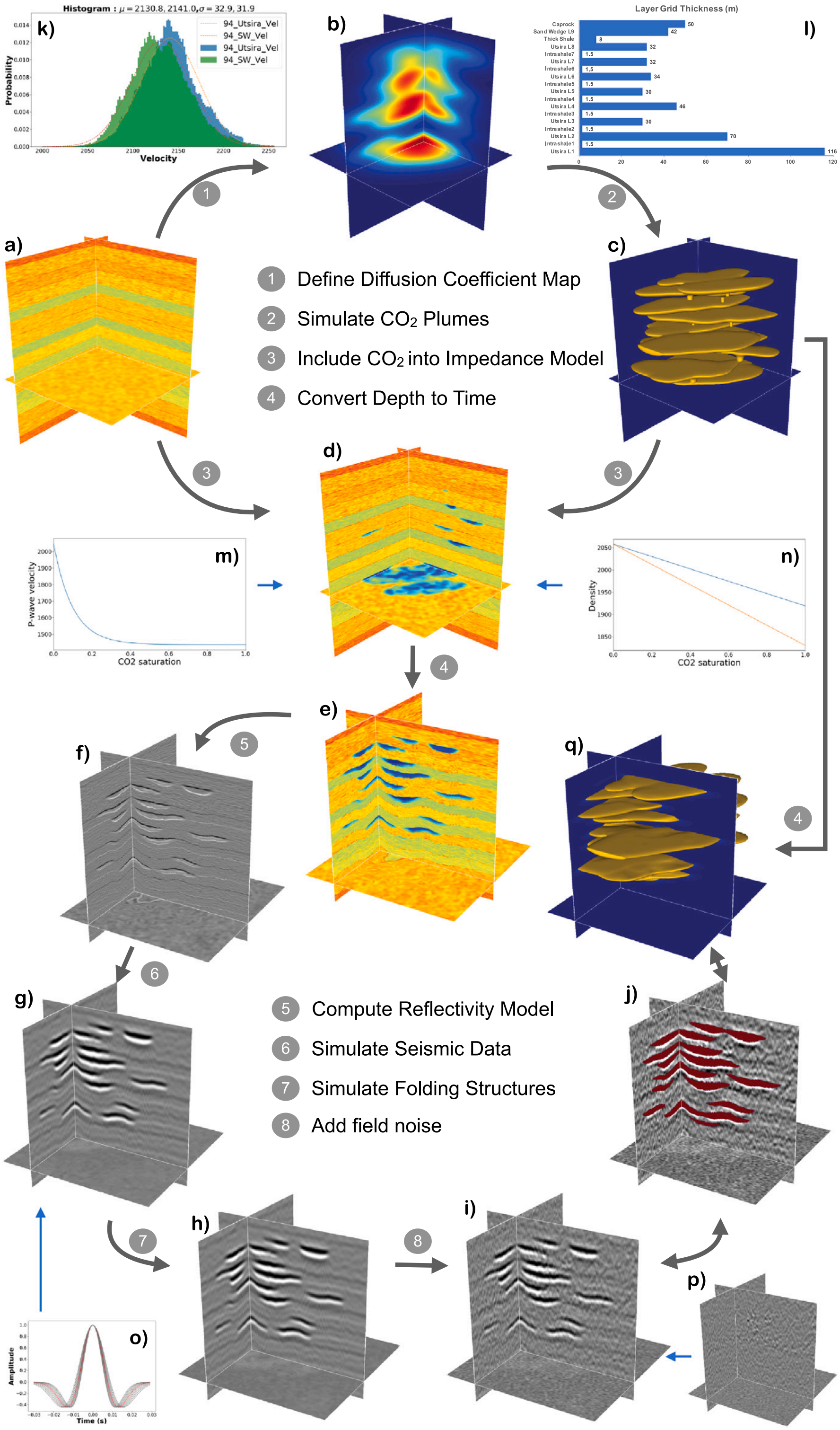

Fig. 3. Workflow of generating the synthetic seismic data and corresponding CO_2 label volume. We first synthesize a flat impedance model (a), where the velocities follow the velocity distribution of Sleipner field statistics including velocity statistics (k) and layer thickness (l). We then simulate a CO_2 diffusion coefficient map (b) and corresponding CO_2 plumes. We modify the impedance values within the simulated CO_2 plumes (d) according to the velocity decay equation (m) and density decay equation (n). After CO_2 injection, we further perform the depth-to-time conversion to obtain the impedance model (e) and CO_2 plumes (q) in the time domain. We then compute the corresponding reflectivity model (f) and further convolve the reflectivity model with a wavelet (o) to simulate seismic data (g). To make the synthetic data more realistic, we implement some folding (h) and add real noise (p) to the synthetic seismic data (i). In this way, we are able to synthesize training dataset pairs of seismic volumes and the corresponding CO_2 labels like the ones in Figures i and j. (For interpretation of the references to color in this figure legend, the reader is referred to the web version of this article.)

the diffusion coefficient map. The irregular ellipsoid areas and lateral variations are helpful to simulate realistic CO_2 plumes with laterally anisotropic shapes.

With the defined diffusion coefficient map determined, we further simulate CO_2 plumes by implicitly solving the diffusion equation as follows [74]:

$$g(\mathbf{x}) - \sigma c(\mathbf{x}) \nabla g(\mathbf{x}) = f(\mathbf{x}), \tag{2}$$

where $g(\mathbf{x})$ represents a volume with CO_2 plumes after diffusion. $f(\mathbf{x})$ is the input volume where CO_2 is initiated at the injection point and feeder paths. Here we include CO_2 at the feeder paths in the initial input to accelerate the diffusion process. $c(\mathbf{x})$ represents the previously defined diffusion coefficient map as shown in Fig. 3b. The constant σ is a parameter that controls the relevant intensity of diffusion. When $\sigma = 0$, Eq. (2) becomes $g(\mathbf{x}) = f(\mathbf{x})$, where no diffusion process is carried out in the initial state. By solving this linear equation using the conjugate gradient algorithm, we are able to simulate the diffusion process in one step to efficiently obtain CO_2 plumes like the one shown in Fig. 3c.

Note that here we are not trying to physically simulate the process of CO_2 migration in the subsurface, which could be highly time-consuming because we need to generate a lot of training datasets. For our problem of characterizing the CO_2 shapes and locations within a seismic image, our simple method is sufficient to simulate the realistic geometries of CO_2 plumes (golden shapes in Fig. 3c) in the subsurface.

3.2.3. Building impedance models with CO_2 plumes

With the impedance model (Fig. 3a) and CO_2 plumes (Fig. 3c) generated, we further modify the impedance values within the simulated CO_2 plumes. The impedance variations introduced by CO_2 plumes results in corresponding changes in both velocities and densities. For the velocity decay function, we use an exponential decay function proposed by Ghaderi and Landrø [75] to indicate the P-wave velocity V_p changes along with CO_2 saturation S:

$$V_p = V_{p1} + V_{p2} e^{-\kappa S}, \tag{3}$$

where $V_{p1} = 1437$ (m/s), $V_{p2} = 613$ (m/s), and $\kappa = 10$. These parameters are estimated by Ghaderi and Landrø [75] through fitting the data with a porosity value of 37%. This Eq. (3) indicates that the velocity decays with CO_2 saturation as shown in Fig. 3m and we apply a similar velocity decay to the initial velocity model where CO_2 plumes occupy.

The density of the rock ρ consists of two parts: the density of the fluid ρ_F and the density of the rock matrix ρ_S. We can formulate these three densities in terms of porosity φ by using the equation:

$$\rho = \varphi \rho_F + (1 - \varphi) \rho_S. \tag{4}$$

According to the statistic data, we set φ to be 0.37 and ρ_S to be 2650 (kg/cm^3). ρ_F is the composed fluid density including both CO_2 fluid and water. So the density of fluid ρ_F can be expressed as a linear combination of these two phases [76]:

$$\rho_F = S \rho_{CO_2} + (1 - S) \rho_W, \tag{5}$$

where S represents the saturation of CO_2, ρ_{CO_2} represents the density of CO_2, and ρ_W represents the density of water. In general, the density of water ρ_W is given as 1050 (kg/cm^3). CO_2 density is sensitive to variations in temperature and pressure. If the temperature increases from 30 to 40 degrees, the density of the CO_2 fluid will decrease from 680 (kg/cm^3) to 300 (kg/cm^3) [76]. Alnes et al. [17] propose the density of CO_2 is 485 (kg/cm^3) where the well-bottom temperature is 48 °C and the fluid pressure is 105 bar. The CO_2 density turns to be 425 (kg/cm^3) when reaching the top Utsira. Alnes et al. [17] conclude that the average density of CO_2 is 675 (kg/cm^3). To include the full range of CO_2 density decay variation, we calculate the variation of rock density ρ with CO_2 saturation S with both the CO_2 density ρ_{CO_2} at 425 (kg/cm^3) (orange line in Fig. 3n) and 675 (kg/cm^3) (blue line in Fig. 3n), respectively:

$$\rho = \varphi (S \rho_{CO_2} + (1 - S) \rho_W) + (1 - \varphi) \rho_S. \tag{6}$$

With two calculated results in Fig. 3n, we are able to obtain the density decay function along with the increase in CO_2 saturation. Besides, the corresponding temperatures and pressures change as the depth increases. Therefore, we also introduce a depth-dependent attenuation compensation factor in the density decay process to make the simulation more realistic and reliable. With the eventual decay equation for velocities and densities with CO_2 saturation, we further apply these decay functions to the impedance model accordingly. The impedance model with CO_2 plumes (Fig. 3d) shows a significant impedance decrease and a distinct lateral variation where CO_2 plumes occupy.

The impedance model in the depth domain can directly reflect the true shape of CO_2 plumes, but the provided Sleipner field seismic images are in the time domain. Therefore, we need to convert the depth-domain impedance model to the time-domain and further generate the corresponding seismic data for training. We use the velocity model and the following equation to calculate the traveltime:

$$t_i = \sum_{i=1}^{n} 2 * d_z / v_i, \tag{7}$$

where t_i represents the traveltime, d_z represents the depth interval (1 m) of the impedance model, and v_i represents the velocity of the ith point in the velocity model. With the calculated traveltime map, we further interpolate the impedance model into the time domain with a 2 ms sampling interval. In this way, we are able to obtain the impedance model in the time domain as shown in Fig. 3e. We can observe a significant bending of the impedance model after the conversion to the time domain, compared to the flat impedance model in the depth domain. In view of the fact that the velocity decays introduced by CO_2 generate longer traveltimes compared to the surrounding velocity. It also means that the shape of the CO_2 plumes obtained on the time-domain seismic image is not consistent with the real one. The related issues are discussed and analyzed in the section of *Seismic Data and* CO_2 *Plumes Registration*.

3.2.4. Simulating synthetic seismic volumes

Through the above processes, we are able to obtain abundant and diverse impedance models containing various CO_2 plumes. We can easily convert the impedance models to reflectivity models (Fig. 3f) and further convolve with a Ricker wavelet (Fig. 3o) to simulate synthetic seismic volumes like the one in Fig. 3g. Furre and Eiken [14] point out that the Ricker 30-Hz wavelet (red curve in Fig. 3o) represents the dominant frequency of the 3-D seismic data in the Sleipner survey. We randomly choose wavelet peak frequencies between 25 Hz to 35 Hz (gray curve in Fig. 3o) for each seismic volume to improve the diversity of synthetic seismic data. Here, we obtain the initial seismic image, but it still differs from the Sleipner field data in terms of folding structures and noise.

Folding is widespread during stratigraphic evolution because sedimentary horizontal layers will suffer an outside force (e.g., plate movement, etc.) and consequently be deformed. Simulating folding structures to the seismic data can make the synthetic data more consistent with the field data. We randomly simulate folding structures by vertically shearing the initial seismic image with the method proposed by Wu et al. [55]. We avoid adding significantly deformed structures of anticlines and synclines so that the dip angles of the layers are not large as shown in Fig. 3h.

Instead of adding random noise, we add noise extracted from field seismic data into our synthetic datasets. We take the 10**p**10 (Fig. 4a) data as an example to illustrate the process of noise extraction as shown in Fig. 4. We first compute smoothed seismic data (Fig. 4b) by using the structure-oriented smoothing method [74]. We then compute the noise data (Fig. 4c) by subtracting the smoothed data from the original one. After obtaining the real noise, we randomly crop a sub-volume with the same size as the synthetic seismic volumes (Fig. 3p) from the full noise volume (Fig. 4c). Note that Fig. 3p is zoomed out in the displaying.

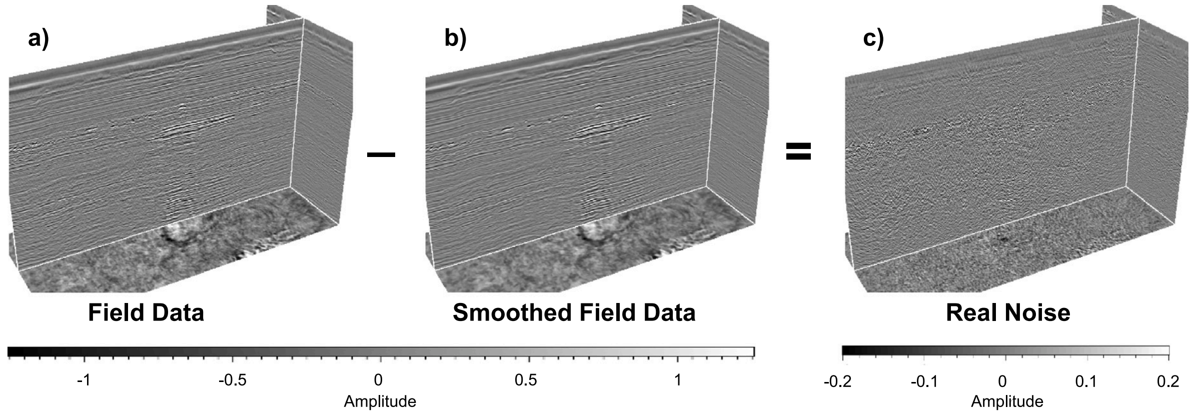

Fig. 4. Workflow of extracting real noise volume from field data. Taking the seismic data 10**p**10 (a) as an example, we first apply a structure-oriented smoothing filter to the original data (a) and obtain the smoothed seismic volume (b). We then obtain the noise volume (c) by subtracting the smoothed volume from the original one.

It has the same size as Fig. 3h. After obtaining a noise volume, we further add it to synthetic seismic data with a noise-to-signal ratio that is randomly defined within the range between 0.1 and 0.9.

By randomly choosing the parameters at each step of the entire workflow (Fig. 3), we can obtain diverse and realistic seismic images with random impedance models, random CO_2 plumes, random wavelets, random folding structures, and a random subset of real noise. The corresponding label volumes for CO_2 plumes are accurate because they are automatically calculated by well-defined equations. We show the CO_2 plumes label overlaid on the seismic in Fig. 3j, where the label values are defined as ones within the CO_2 plumes while zeros elsewhere. In total, we obtain 400 pairs of 3-D seismic volumes and their corresponding CO_2 plumes label volumes like those shown in Fig. 5. Fig. 5 shows four seismic volumes (the first row) and their corresponding label volumes in 2-D (the second row) and 3-D (the second row) overlaid view. These diverse seismic images and the corresponding labels can enable the neural network learns to accurately detect CO_2 features.

In addition to the synthetic datasets (Fig. 6a and b), we also randomly crop 16 pairs of field training datasets (Fig. 6c) from the baseline field seismic data before CO_2 injection. The CO_2 label volumes for these real datasets are zeros everywhere as shown in Fig. 6d. In this way, we obtain a combination of mixed training datasets (Fig. 6) where the synthetic datasets (Fig. 6a and b) tell a neural network to detect all possible CO_2 features while the field ones (Fig. 6c and d) tell the network to avoid mis-detecting the features resembling the true CO_2 features. In addition, we implement the same workflow to generate validation datasets containing 100 pairs of 3-D seismic volumes.

4. CNN-based CO_2 characterization

After finishing the preparation of the training datasets, we then introduce the network architecture trained for characterizing CO_2 plumes in 3-D seismic volumes. In addition, several strategies are applied while training our network, such as data augmentation, loss function, learning rate scheme, etc. After the training is completed, we show the feature maps of each layer in our network, the loss unction curves, and the prediction results in the validation datasets to demonstrate the effectiveness of our method.

4.1. Network architecture

We consider the CO_2 plumes characterization in 3-D seismic volumes as an image segmentation problem and we solve the problem by using a neural network based on U-net [34], which has been widely used in image segmentation problems in various fields. The architecture of our network (Fig. 7) consists of an encoder–decoder architecture, which includes four downsampling kernels and the corresponding upsampling kernels. Each downsampling kernel in our network contains two $3 * 3 * 3$ kernel convolutional layers with a rectified linear unit (ReLU) and one $2 * 2 * 2$ kernel max-pooling layer. After four downsampling blocks, the number of feature channels changes from 32 to 64, 128, 256, and 512, respectively. These features obtained from different downsampling blocks are connected to the corresponding upsampling layers at the same level by skip-connection operators. The skip-connection operators aim to fuse both high-level and low-level features obtained in the encoder stage (lower-left part in Fig. 7) to the decoder stage (lower-right part in Fig. 7). Every corresponding upsampling kernel in the decoder stage contains one $2 * 2 * 2$ kernel up-sampling layer and two $3 * 3 * 3$ kernel convolutional layers with a ReLU. After four upsampling blocks, the number of feature channels changes from 512 to 256, 128, 64, and 32, respectively.

4.2. Training and validation

Utilizing our mixed training datasets (Fig. 6), we can train the 3D deep neural network (Fig. 7) for characterizing CO_2 in time-lapse seismic images. The sizes of the input mixed training datasets and the corresponding label volumes for our network are $240 * 192 * 192$. Before feeding the data into the network, we pre-process the training samples to make the training process more robust and obtain a better model. The first step is mean–variance normalization (subtracting the mean value of the sample and dividing the whole sample by its variance afterward). Secondly, we rotate the seismic volume and its corresponding CO_2 label volume around the z axis to further increase the diversity of training data. The rotation is chosen randomly from 90, 180, and 270 degrees. In this way, each training data pair in our training datasets becomes two pairs when feeding into the network: the original data and the rotated one.

We regard the CO_2 detection problem as a regression problem, and use Mean-Square Error (MSE) as the loss function:

$$\mathcal{L}_{MSE} = \frac{1}{N}\sum_{i=1}^{N}\left(\mathbf{x}_i - \mathbf{y}_i\right)^2, \tag{8}$$

This loss function $\mathcal{L}_{MSE}$ is the average of the squared differences between the predicted $\mathbf{x}_i$ and labeled $\mathbf{y}_i$ data. N represents the total number of samples in the labeled data ($240 * 192 * 192$). The optimization method for our network is the Adam method [77] with a learning rate of 1e–4 at the beginning. To better optimize the loss in the late training process, we choose a learning rate scheme that reduces the learning rate to one fifth of the original when the loss does not decline for a duration of four epochs. The loss and accuracy curves on training (the blue curve) and validation (the orange curve) datasets are shown in Fig. 8. Here, we show the prediction results (the second row in

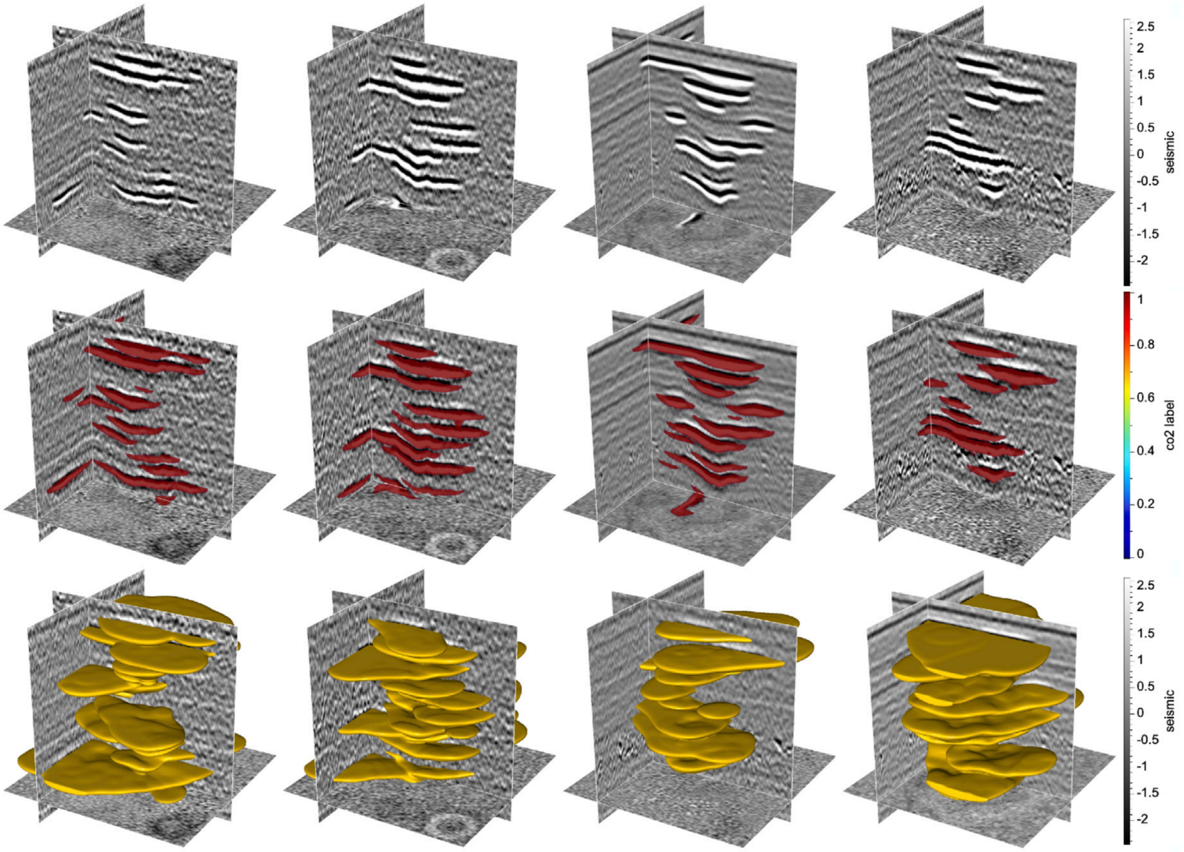

Fig. 5. We show four synthetic seismic data (the first row) obtained by our synthetic workflow (Fig. 3) and the corresponding CO_2 label volumes. The label volumes are shown in both 2-D (the red area in the second row) and 3-D (the third row) views. (For interpretation of the references to color in this figure legend, the reader is referred to the web version of this article.)

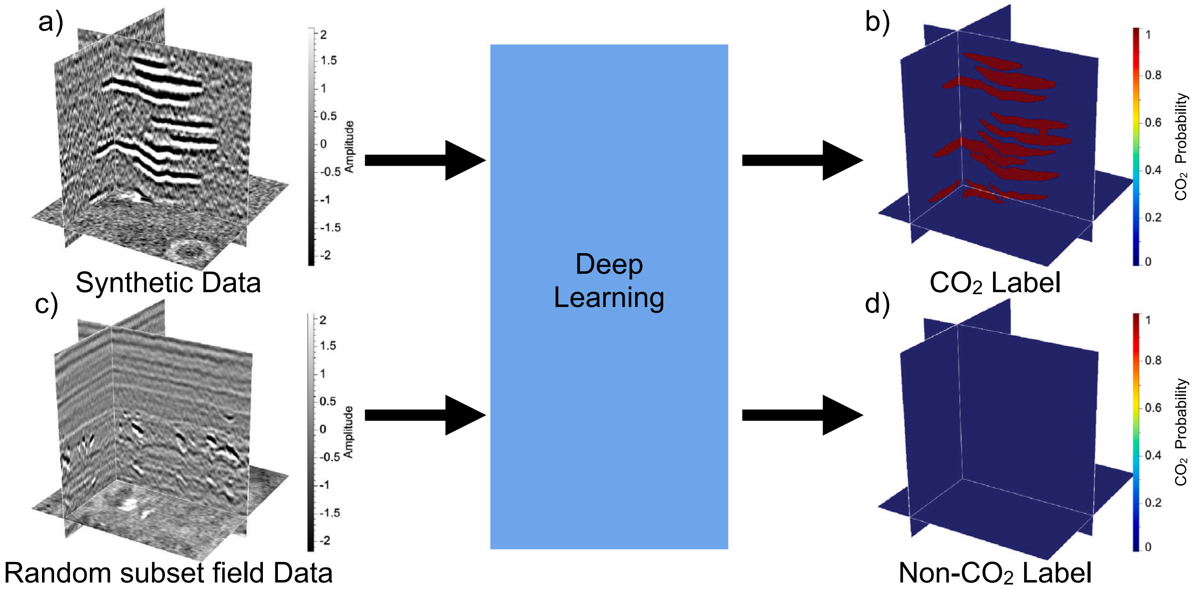

Fig. 6. The entire training datasets consists of two subsets including synthetic datasets and field datasets. The synthetic datasets contain abundant and diverse synthetic seismic data (a) using stochastic simulation and seismic forward modeling. The corresponding CO_2 label volume (b) within synthetic datasets is accurate. The field datasets contain a set of field seismic volumes (c) with empty CO_2 plumes that are randomly cropped from the field baseline data without CO_2 injection. The corresponding CO_2 label volume (d) within field datasets are filled with all zeros.

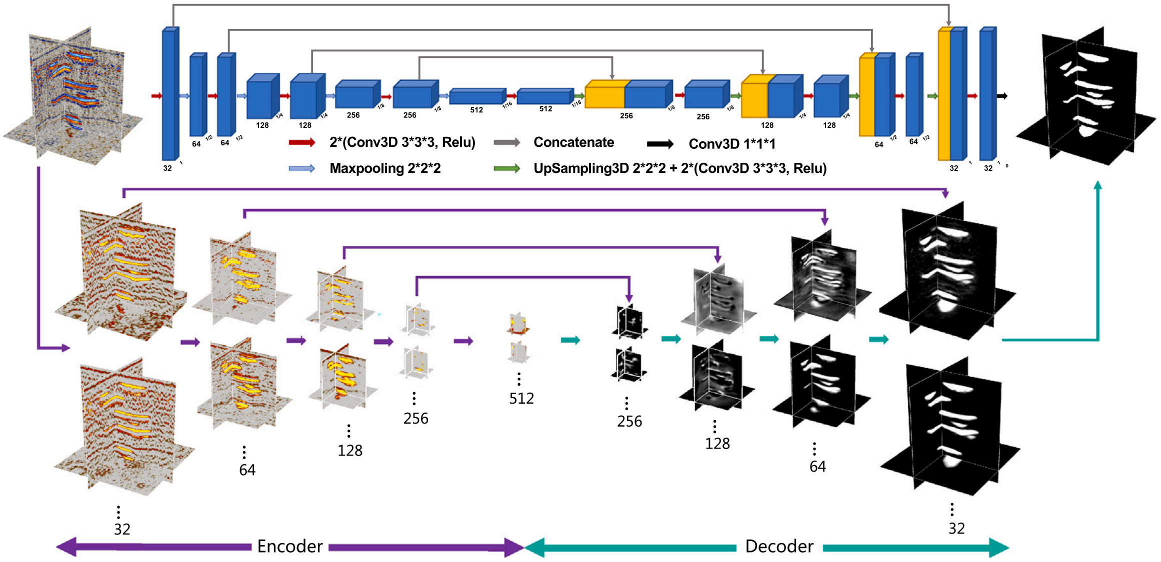

Fig. 7. The network architecture used in our method (the upper part) and the corresponding features (the upper part) in each layer. The feature map shows that the encode stage continuously extracts features about CO_2 from the seismic data and the decode stage gradually approximates the features toward the label volume.

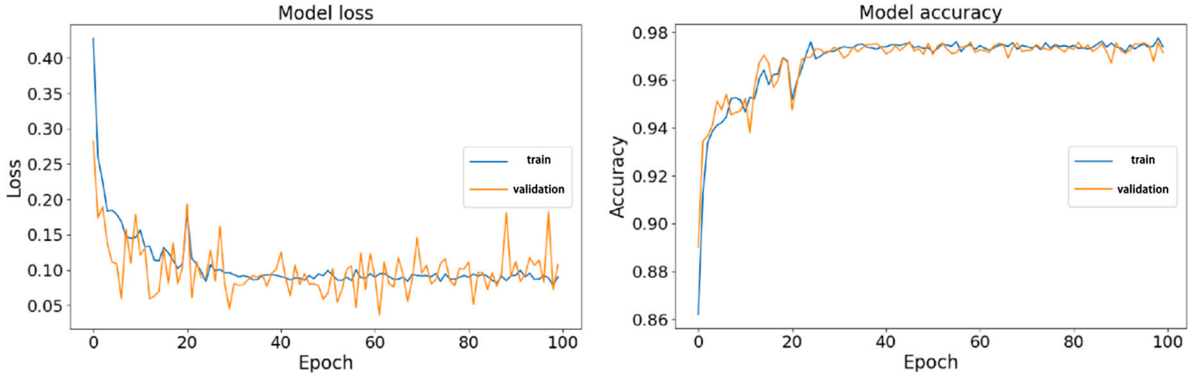

Fig. 8. The loss curves (a) and accuracy curves (b) for both training (blue) and validation (orange). (For interpretation of the references to color in this figure legend, the reader is referred to the web version of this article.)

Fig. 9) for the four seismic data (the first row in Fig. 9) in the validation datasets which are not involved in the training. We can observe that the prediction results are in good agreement with the true labels (the third row in Fig. 9), which also means our method can extract accurate CO_2 features from seismic volumes.

To understand the training process of the network better, we show the feature maps (the lower part in Fig. 7) of each layer in the network. We can observe that the encode stage continuously extracts features about CO_2 from the seismic data and the decode stage gradually approximates the features toward the label volumes. The Encoder stage extracts features related to the strong amplitudes, which is consistent with our previous knowledge of the response of the injected CO_2. Afterward, in the decoder stage, we can observe that the unrelated noise gradually decays and the features fit the CO_2 label volume.

5. Field data applications

We take the Sleipner time-lapse seismic data published by Equinor [69] as an example to test the effectiveness of our method. We selected 99**p**01, 01**p**07, 04**p**07, 06**p**07, 08**p**08, and 10**p**10 as the input of our network. Since we did not freeze the input size of the network, we can input seismic data of any size into the network. With an input seismic volume of 256 × 512 × 256 samples, our network can efficiently predict CO_2 plumes, which takes around 29 s by using one graphics processing unit (GPU). Fig. 10 show a 3-D view of the predicted CO_2 probability volumes for 99**p**01, 01**p**07, 04**p**07, 06**p**07, 08**p**08, and 10**p**10 which are overlaid with the corresponding seismic volumes. Fig. 11 shows the 3-D bodies of CO_2 plumes that are extracted from the CO_2 probability volumes (Fig. 10) by using the marching cubes algorithm [78]. The 3-D view of the predicted results clearly show the growth of CO_2 plumes under the subsurface along with the continuous injection of CO_2.

In order to better verify the accuracy and reliability of our method, we compare our results with manual interpretation and a traditional method. Equinor [4] provides the boundary of the CO_2 plume in 9 layers (as denoted by yellow curves in Figs. 12 and 13) with manual interpretation. We take a window in the time direction and calculate the average of the absolute amplitude difference between 94**p**10 and 10**p**10 to indicate the location of the CO_2 plumes [65]. This traditional method, which relies on absolute amplitude anomalies, can only provide rough CO_2 locations and boundaries in time slices as shown in the first row of Fig. 12. Compared with the manual interpretation results enclosed by the yellow curves, the traditional method does not satisfy the requirements for further analysis.

Unfortunately, Equinor [4] does not provide nine layers in the time domain and the corresponding thickness of the CO_2 plumes. Therefore we pick 9 layers using the horizon extraction method [79] with some manually defined control points. Since the picked horizons may not perfectly match the geologic layers and the shale layers within Utsira

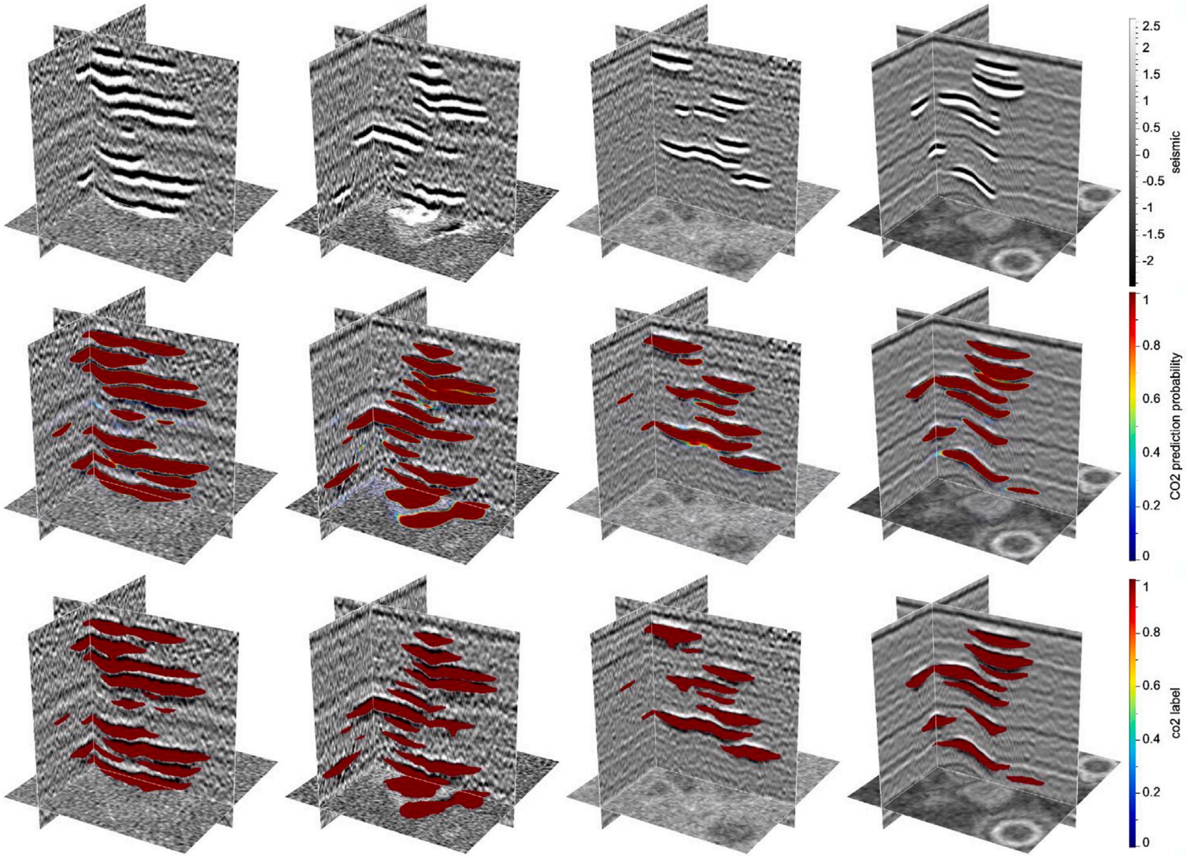

Fig. 9. We show four seismic data (the first row) from validation datasets and their corresponding CO_2 prediction results with our method (the red area in the second row). Our results are consistent with the ground-truth CO_2 features (the red area in the third row). (For interpretation of the references to color in this figure legend, the reader is referred to the web version of this article.)

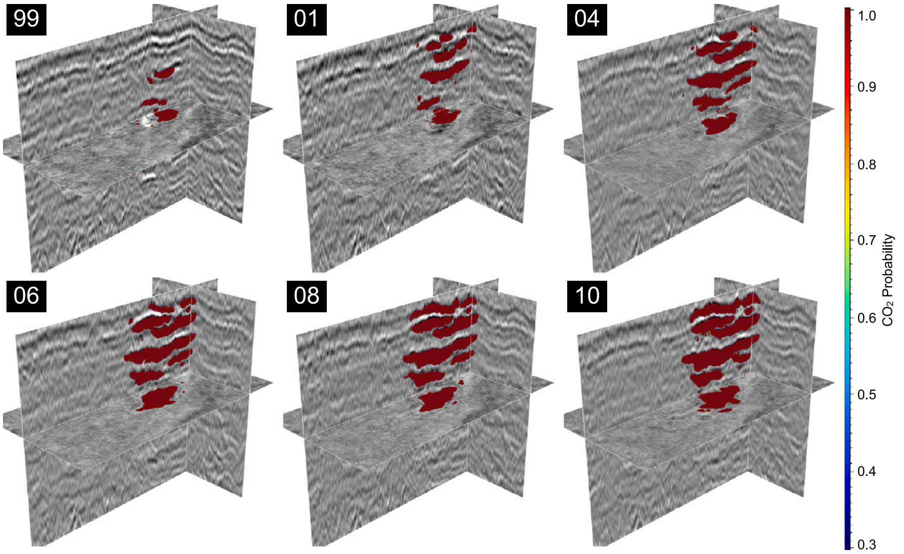

Fig. 10. By applying the trained CNN model to the seismic data of 99**p**01, 01**p**07, 04**p**07, 06**p**07, 08**p**08 and 10**p**10, we obtain the corresponding CO_2 probability volumes overlaid with the seismic volumes.

Formation are not continuous, we compute the average of the predicted CO_2 probability over a time window (centered at the horizons) and display the averaged probabilities overlaid with the horizon slices in the second row of Fig. 12. Compared to the results of the traditional method in the first row of Fig. 12, our results are more consistent with the manually interpreted labels. Further, we quantitatively evaluate the results of our predictions compared to manual labeling. The accuracy and mean Intersection over Union (mIoU) metrics for each layer are shown in the Table 2. Accuracy can indicate the percentage of points that are accurately classified. mIoU can indicate the average overlap ratio between the area occupied by the predicted CO_2 and the labeled CO_2 area. All of our predicted results can achieve more than 95% accuracy and more than 0.8 mIoU score. It means that our method can simultaneously balance the efficiency with the accuracy.

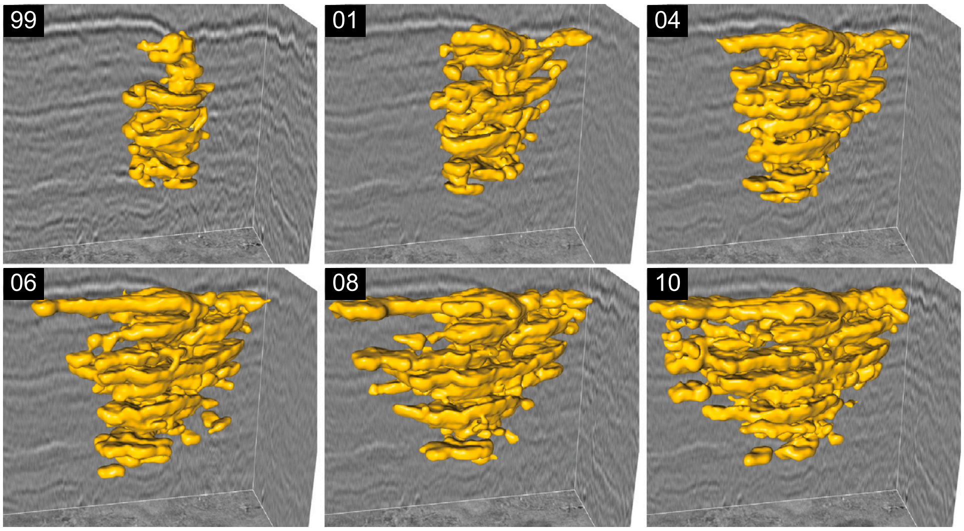

Fig. 11. From the CO_2 probability volumes predicted from the seismic data of 99**p**01, 01**p**07, 04**p**07, 06**p**07, 08**p**08 and 10**p**10, we are able to automatically extract the 3-D CO_2 plumes bodies (colored by yellow) by using the marching cubes method. (For interpretation of the references to color in this figure legend, the reader is referred to the web version of this article.)

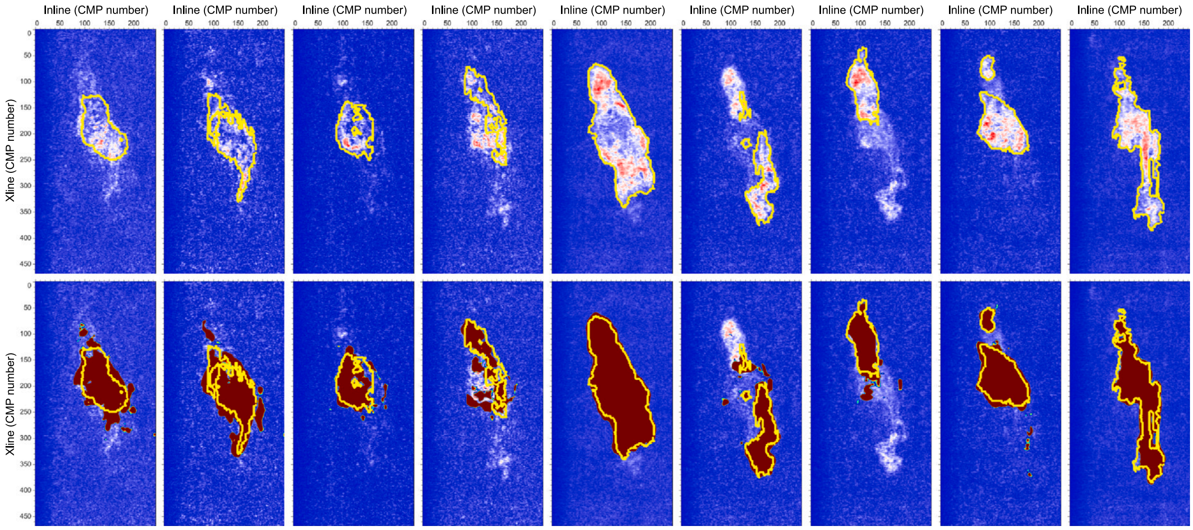

Fig. 12. The traditional results (the first row) and our prediction results (the second row) of 10**p**10 within corresponding nine layers. The yellow curves are manually interpreted as CO_2 boundaries by Equinor [69]. (For interpretation of the references to color in this figure legend, the reader is referred to the web version of this article.)

Table 2
The accuracy and mean IoU of our prediction results.

Layer	1	2	3	4	5	6	7	8	9	Average
Accuracy	0.9597	0.9650	0.9649	0.9598	0.9596	0.9561	0.9548	0.9513	0.9515	0.9581
Mean IoU	0.8517	0.8546	0.8483	0.8327	0.8584	0.8404	0.8339	0.8183	0.8130	0.8390

In addition to the predicted CO_2 probabilities on the nine layers of 10**p**10, we can also obtain the CO_2 probabilities on the nine layers in all the seismic volumes of 99**p**01, 01**p**07, 04**p**07, 06**p**07, and 08**p**08 from which we are able to analyze the migration of CO_2 with time. The first row of Fig. 13 shows the results of 10**p**10, where the results are in good consistent with the manual interpretation (yellow lines). The amplitude within CO_2 plumes in the lower layers may be relatively weak compared to the surroundings, which could be influenced by the temperature and pressure changes at different depths or the errors introduced by seismic processing.

We further show the full-layered results in time-lapse seismic images to observe the migration of CO_2 plumes including 08**p**08 (the second row in Fig. 13), 06**p**07 (the third row in Fig. 13), 04**p**07 (the fourth row in Fig. 13), 01**p**07 (the fifth row in Fig. 13), and 99**p**01 (the sixth row in Fig. 13). We can clearly observe that the CO_2 plumes increase over time. Besides, the prediction results of CO_2 plumes are in good agreement with the results of Li and Li [65]. The growth of the CO_2 plumes shown in Fig. 13 is consistent with the physical law: CO_2 migrates upward due to buoyancy and diffuses along with the layers. With the buoyancy driving, the lower layers are in a slower growth rate compared to the top layer, which is consistent with the observations by Arts et al. [13]. We can also observe that the amount of CO_2 plumes in the ninth layer is relatively small in 1999 because CO_2 has just reached the top layer at that time [24].

Another important analysis is about the CO_2 feeders. If the threshold pressure of injected CO_2 exceeds a certain value, the CO_2 plumes may

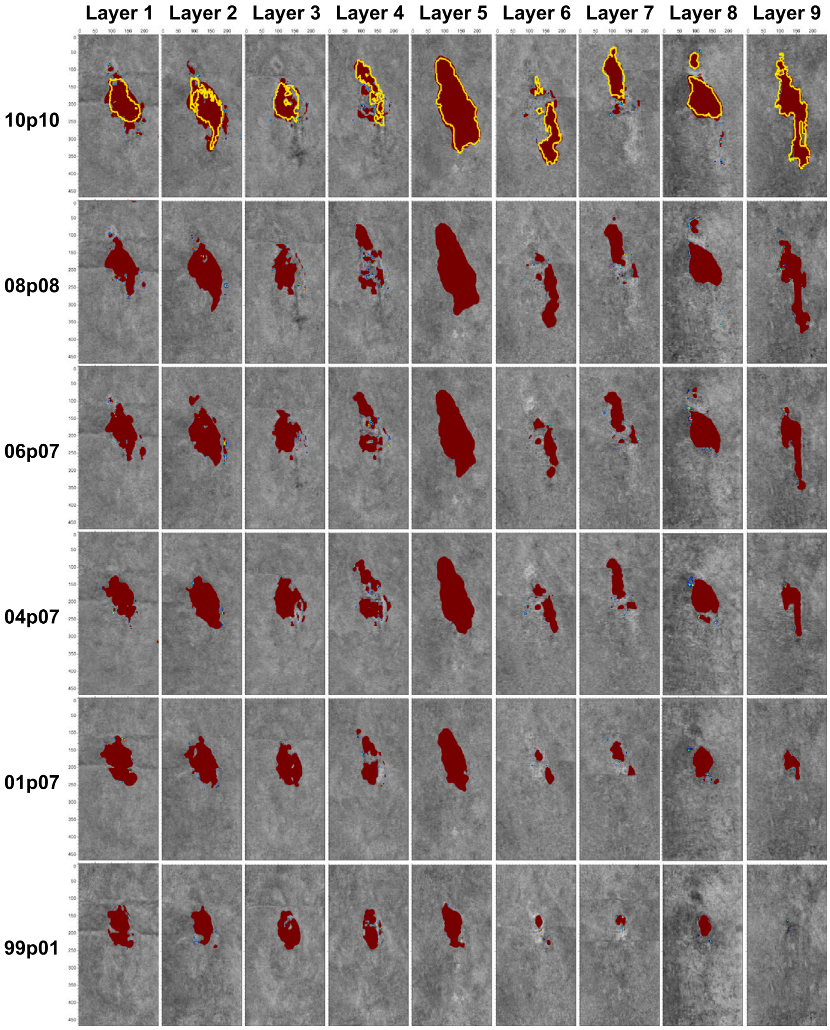

Fig. 13. The predicted CO_2 results shown in nine layers for 10**p**10 (the first row), 08**p**08 (the second row), 06**p**07 (the third row), 04**p**07 (the fourth row), 01**p**07 (the fifth row), and 99**p**01 (the sixth row), respectively. (For interpretation of the references to color in this figure legend, the reader is referred to the web version of this article.)

break through the shale from the sandstone upwards, thus forming a chimney [29]. Detecting such chimneys is typically difficult in individual seismic data and it requires the analysis of year-by-year seismic data [80]. The North-eastern feeder (Layer 5 to Layer 6) and the South-western feeder (Layer 7 to Layer 8) are two typical feeders which have been proved by many scholars and published in the Equinor reference model [4].

The evidence of the North-eastern feeder (Layer 5 to Layer 6) is that the initial emergence location and the main growth direction of the sixth layer do not have any correlation with the injection point. Therefore, many scholars believe that CO_2 migrates from Layer 5 to Layer 6 through the North-eastern feeder, which leads to the growth of Layer 6 to deviate from the injection point. Our prediction results in Fig. 13 are consistent with the above analyses. In the sixth layer (the sixth column in Fig. 13), the CO_2 plume located near the injection point does not show a significant increase along with the CO_2 injection. While the CO_2 plumes in the lower-right of the sixth layer appear to be growing visibly, which indicates the CO_2 migration is at a certain distance from the injection point. Thus, our prediction results prove that CO_2 migrates from Layer 5 to Layer 6 through the chimney.

The south-western feeder (Layer 7 to Layer 8) can be confirmed by observing that the growth of the two individual parts in layer 8 (the eighth column in Fig. 13) is not connected and correlated. We can observe that the larger region is continuously exaggerated from 1999 to 2010. However, the smaller region suddenly appears and starts to expand since 2006, which does not correlate well with the CO_2 in the large region. We can figure out that our results (the eighth column in Fig. 13) are consistent with the previous analysis. These analyses of CO_2 migration and the two chimneys further verifies that the results of our method are physically consistent and reliable.

6. Seismic images and the corresponding CO_2 plumes registration

Our deep learning method can characterize CO_2 plumes in time-lapse seismic images for analyzing CO_2 migration. However, the CO_2 plumes in time-lapse seismic images are not consistent with the true CO_2 shape in the subsurface as discussed in the section of *Synthetic Training Datasets*. They will be affected by the acquisition inconsistency, processing inconsistency, velocity changes (push-down effects), and wavelet distortion (pull-up effects). We will discuss how to solve these problems to obtain CO_2 plumes whose shapes are more consistent with the real ones.

As we discussed in the section of *Geologic Background and Datasets of the Sleipner Survey*, the time-lapse seismic data are acquired with slightly different acquisition geometries in different years, We show the seismic surveys of 99**p**01 (blue), 06**p**07 (yellow), and 10**p**10 (orange) in Fig. 14. The seismic surveys of 01**p**07 and 04**p**07 are consistent with 06**p**07, which are shown as the yellow region in Fig. 14. The seismic survey of 08**p**08 is consistent with 10**p**10, which is the orange region in Fig. 14. Characterizing CO_2 migration with time-lapse seismic

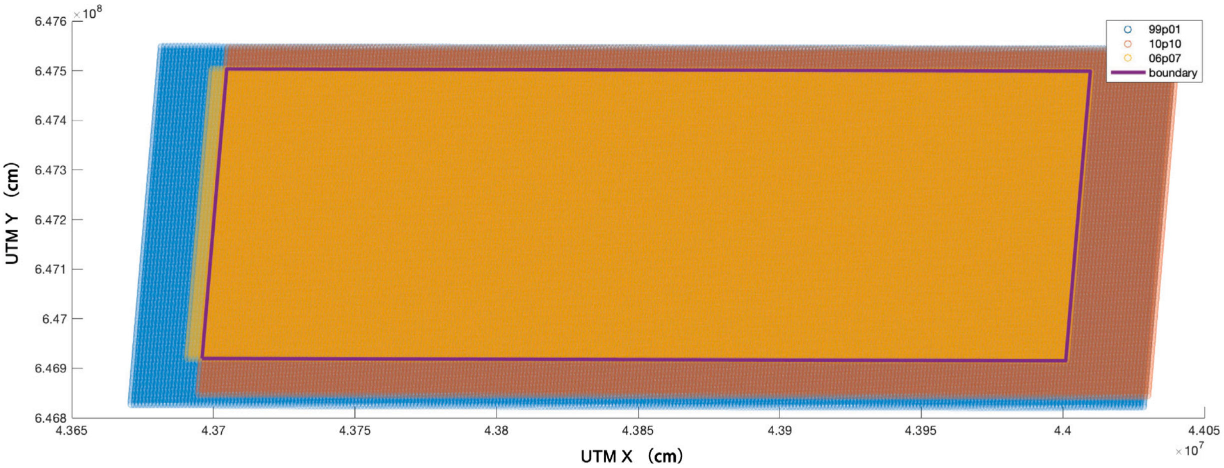

Fig. 14. The seismic surveys map of 99**p**01 (blue), 06**p**07 (yellow) and 10**p**10 (orange) in Fig. 14. The seismic surveys of 01**p**07 and 04**p**07 are consistent with 06**p**07, which are also the yellow area in Fig. 14. The seismic survey of 08**p**08 is consistent with 10**p**10, which is also the orange area. The purple box shows the boundary of the intersection of all seismic surveys. (For interpretation of the references to color in this figure legend, the reader is referred to the web version of this article.)

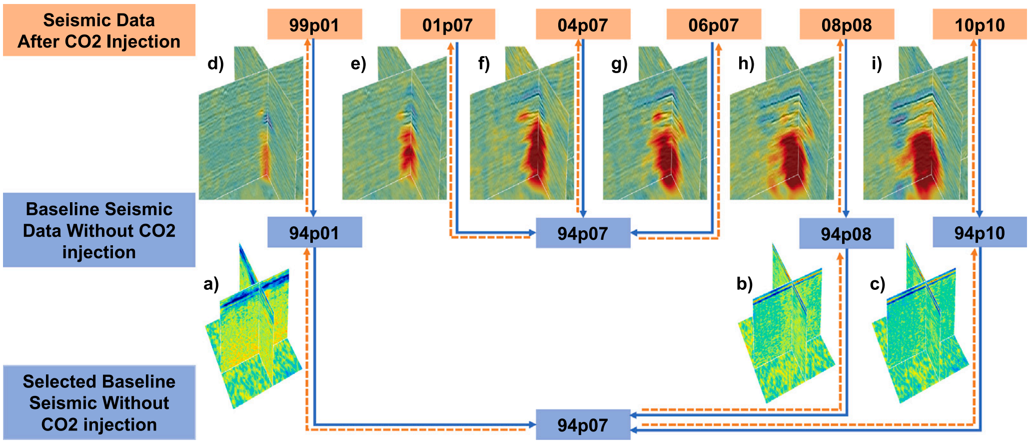

Fig. 15. The workflow of seismic data registration. We first match the baseline data 94**p**01, 94**p**08, and 94**p**10 with the baseline data 94**p**07 by the *Dynamic image warping* (*DIW*) method. We can obtain the respective time shift (a, b, and c), which we consider as the time shift caused by processing. In this way, all baseline seismic data are consistent with the 94**p**07 in position. We then apply the *DIW* method to match seismic data after CO_2 injection including 10**p**10, 08**p**08, 06**p**07, 04**p**07, 01**p**07, and 99**p**01 with their corresponding registered baseline seismic volume. By doing this, we have achieved that all seismic data after CO_2 injection are registered to the same baseline data (94**p**07).

datasets involves multiple seismic data, and the acquisition geometries may not be consistent. Some of the CO_2 spatial migration changes we observed from multiple time-lapse seismic data may be due to the inconsistency of the acquisition geometries. In order to reduce the uncertainty caused by these acquisition geometries, we need to exclude this observation system inconsistency and obtain a more objective reflection of subsurface CO_2 migration. We take the overlaying area (bounded by the purple rectangle) as a new survey and re-grid all the seismic data in this new survey. By doing this, all the time-lapse seismic data are resampled in a shared survey with the same acquisition geometry and we are able to eliminate the CO_2 uncertainties caused by the acquisition variations over time.

As shown in Table 1, the time-lapse seismic data are not processed under the same baseline data, which introduces uncertainties or inconsistencies in the seismic images. Besides, the injection of CO_2 will decrease the corresponding velocity, thus leading to some structural artifacts. This effect lead to a push-down effect in the layers below [81]. Furre et al. [22] also point out the wavelet distortion will cause an apparent pull-up at the top reflector for a CO_2 thickness below 8 m. To eliminate the potential errors introduced by processing, push-down effect, and pull-up effect, we propose a workflow (Fig. 15) to register seismic images and the corresponding CO_2 plumes.

To reduce the inconsistency of baseline data, we first choose the baseline data 94**p**07 as the reference and register all the other baseline data 94**p**01, 94**p**08, and 94**p**10 to the reference by using the *Dynamic images warping* (*DIW*) method [82]. Fig. 15a, b, and c show the estimated time shifts for the data 94**p**01, 94**p**08, and 94**p**10, respectively, which can be considered as the inconsistencies caused by data processing at different years. We can apply the estimated time shifts to the corresponding seismic data to eliminate the inconsistencies caused by data processing. In this way, all baseline seismic data (without CO_2 injection) are vertically aligned with the baseline data of 94**p**07.

We then apply the *DIW* method to align seismic data after CO_2 injection including 10**p**10, 08**p**08, 06**p**07, 04**p**07, 01**p**07, and 99**p**01 with their corresponding registered baseline data. We take the data pair of 01**p**07 (Fig. 16b) and 94**p**07 (Fig. 16a) as an example to illustrate the registration process. First, we calculate alignment time shifts (Fig. 16c) between 01**p**07 and 94**p**07 by using the DIW method. Hale [82] smooth alignment errors along all three image dimensions before eventually using DTW to estimate the shifts. The DTW method is then applied to find the optimal alignment time shift. From the time shift, we are able to observe that the time shifts caused by push-down effect (the downward bending below CO_2 plumes) and pull-up effect (the upward bending at the top CO_2 plumes) are also consistent with the previous studies. We then apply the calculated time shift to 01**p**07 and obtain the warped data shown in Fig. 16d. We also compute the difference (Fig. 16f) between the warped 01**p**07 and 94**p**07 and the difference

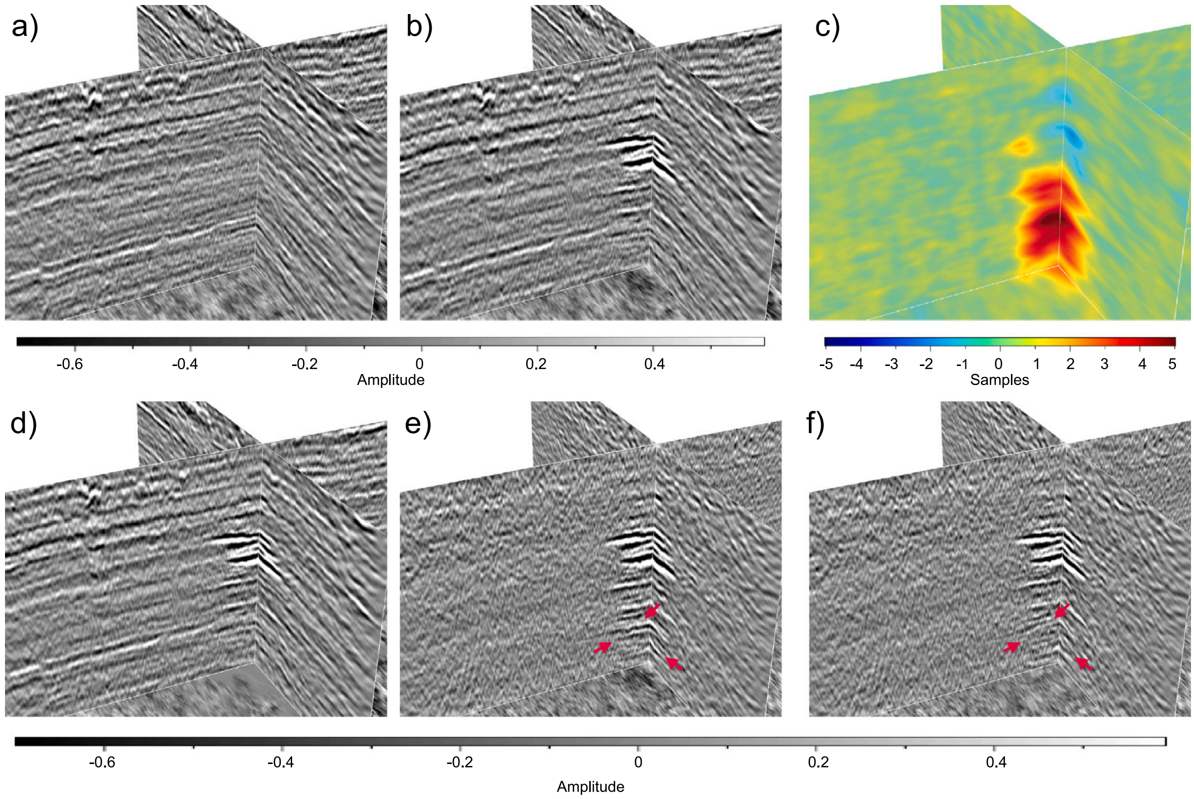

Fig. 16. An example of seismic registration with the DIW method. Taking the baseline seismic data 99p01 as the reference volume, we compute the registration time shifts (c) that align the seismic volume 01p07 (b) to the reference one (a). By applying the estimated time shifts to the seismic volume 01p07 (b), we further obtain the registered seismic volume in (d). We also compute the difference (f) between the warped 01**p**07 and 94**p**07 and the difference (e) between the original 01**p**07 and 94**p**07. We can observe some strong amplitudes (denoted by red arrows) corresponding to the push-down effect are weakened after the registration in (f), which is helpful to avoid mis-interpreting these features as CO_2. (For interpretation of the references to color in this figure legend, the reader is referred to the web version of this article.)

(Fig. 16e) between the original 01**p**07 and 94**p**07. We can observe some strong amplitudes as denoted by the red arrow in Fig. 16e due to the push-down effect, which may be mis-detected as CO_2 plumes. While the amplitude differences after registration (Fig. 16f) become weaker in the corresponding region and do not generate continuously visible reflectors, which indicates that our method can effectively reduce the push-down effect.

Afterward, we apply the same sifts to register the corresponding CO_2 plumes. Fig. 17 shows inline section (extracted from 06**p**07) before (left) and after warping (right). The yellow arrows in Fig. 17 indicate the CO_2 plumes move upwards after warping, which indicates that our registration process might be helpful to reduce the push-down effect and recover the actual shape of the CO_2 plumes. On the other hand, the white arrows in Fig. 17 indicate our registration process is also helpful to reduce the pull-up effects. After reducing the acquisition inconsistency, processing inconsistency, velocity changes (push-down effects), and wavelet distortion (pull-up effects), we are able to obtain CO_2 plumes whose shapes are more consistent with the real ones.

7. Discussion and conclusion

We propose a deep learning method to automatically characterize CO_2 migration in time-lapse seismic images. Experiments from multiple perspectives show that our method achieves efficiently detection of CO_2 in time-lapse seismic data while ensuring the accuracy. In order to achieve this goal, we have addressed the following main challenges of applying deep neural networks for CO_2 detection. One of the great challenges for neural networks is the lack of labeled datasets. We firstly solve the great challenge of the lacking of labeled dataset by proposing propose a workflow to synthesize seismic data of diffusive CO_2 plumes with different shapes, sizes, and locations for training deep neural networks. With stochastic simulation and seismic forward modeling based on geological background and petrophysical statistics, we are able to obtain diverse and reasonable synthetic training datasets with accurate labels. Another challenge is that utilizing synthetic data to train neural networks encounters poor generalization in field data. To improve the generalization of the neural network, we include the baseline field data before CO_2 injection into the training datasets to allow the network to recognize the structural information of the field survey and keep the network away from incorrect prediction. In this way, we can obtain a combination of mixed training datasets where the synthetic datasets tell our neural network to detect all possible CO_2 features while the field ones tell our network to avoid mis-detecting the features resembling the true CO_2 features.

The application of time-lapse seismic images from the Sleipner indicates that our method is consistent with the manual interpretation. Limited by the cost of manual interpretation, the CO_2 plumes on the manually interpreted nine layers only exist within one seismic data. With our CNN-based model, we can provide the CO_2 plumes over 9 layers within every time-lapse seismic data. Besides, the 3-D view of our predicted results clearly show the growth of CO_2 plumes under the subsurface along with the continuous injection of CO_2. The observations in our results are consistent with the previous studies.

Some limitations remain in our method. One limitation is related to the simulated synthetic training datasets. We simulate the training datasets in this study based on the statistic data (e.g., velocity, density, frequency) in the Sleipner survey. This indicates that the CNN trained by these training datasets might not work well for other field surveys. Fortunately, our workflow allows us to quickly generate training samples that are compatible with a new field survey.

To obtain a more consistent CO_2 plumes migration model, we use the DIW method to register all the time-lapse seismic volumes with

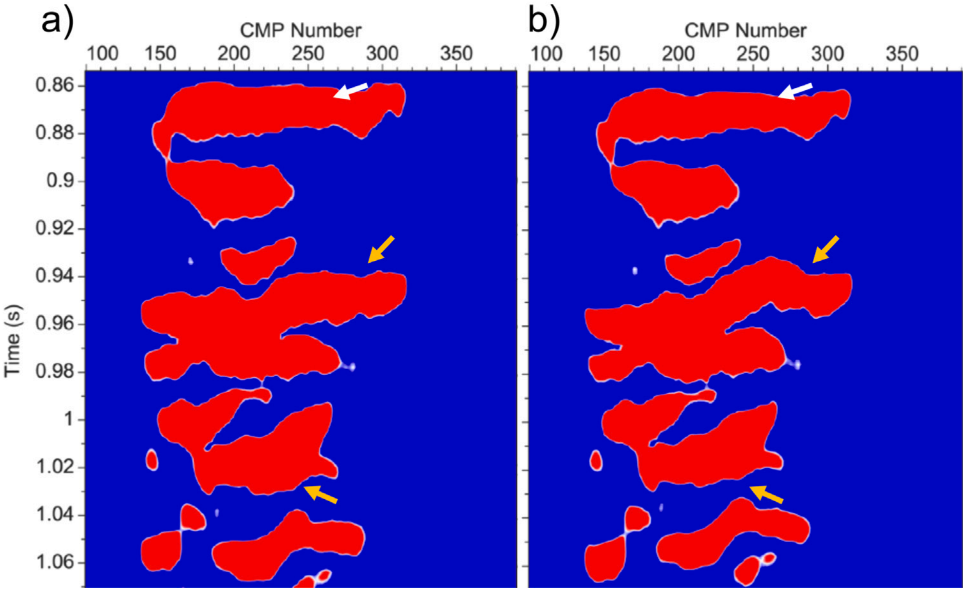

Fig. 17. The predicted CO_2 plumes before (a) and after (b) applying the seismic registration shifts estimated by the DIW method. The yellow arrows indicate that CO_2 plumes move upwards because the push-down effect is reduced by applying the seismic registration shifts. (For interpretation of the references to color in this figure legend, the reader is referred to the web version of this article.)

the baseline seismic volume and also apply the registration shifts to the predicted CO_2 plumes. By doing this, we are able to reduce the inconsistencies caused by acquisition, processing, velocity variations (push-down effects), and wavelet distortion (pull-up effects), which is helpful to obtain a more accurate CO_2 plume migration model.

CRediT authorship contribution statement

Hanlin Sheng: Conceptualization, Methodology, Validation, Formal analysis, Investigation, Resources, Writing – original draft, Visualization. **Xinming Wu:** Conceptualization, Methodology, Investigation, Writing – review & editing, Funding acquisition, Visualization. **Xiaoming Sun:** Validation, Formal analysis, Resources, Writing – review & editing. **Long Wu:** Resources, Writing – review & editing.

Declaration of competing interest

The authors declare that they have no known competing financial interests or personal relationships that could have appeared to influence the work reported in this paper.

Data availability

Data will be made available on request.

Acknowledgments

This research was supported by the National Science Foundation of China under grant no. 41974121.

References

[1] Sepehri A, Sarrafzadeh MH. Effect of nitrifiers community on fouling mitigation and nitrification efficiency in a membrane bioreactor. Chem Eng Process-Process Intensif 2018;128:10–8.

[2] Sepehri A, Sarrafzadeh MH. Activity enhancement of ammonia-oxidizing bacteria and nitrite-oxidizing bacteria in activated sludge process: metabolite reduction and co2 mitigation intensification process. Appl Water Sci 2019;9:1–12.

[3] Sepehri A, Sarrafzadeh MH, Avateffazeli M. Interaction between chlorella vulgaris and nitrifying-enriched activated sludge in the treatment of wastewater with low c/n ratio. J Clean Prod 2020;247:119164.

[4] Equinor. Sleipner 2019 benchmark model. 2020, http://dx.doi.org/10.11582/2020.00004, Retrieved from https://co2datashare.org/dataset/e6f67cbd-abf3-4d85-a118-ed386a994c2c.

[5] Preston C, Monea M, Jazrawi W, Brown K, Whittaker S, White D, Law D, Chalaturnyk R, Rostron B. Iea ghg weyburn co2 monitoring and storage project. Fuel Process Technol 2005;86:1547–68.

[6] Mathieson A, Midgley J, Dodds K, Wright I, Ringrose P, Saoul N. Co 2 sequestration monitoring and verification technologies applied at Krechba, Algeria. Lead Edge 2010;29:216–22.

[7] Zweigel P, Arts R, Lothe AE, Lindeberg EB. Reservoir geology of the utsira formation at the first industrial-scale underground co2 storage site (Sleipner area, North sea). Geol Soc Lond Spec Publ 2004;233:165–80.

[8] Hansen H, Eiken O, Aasum T. Tracing the path of carbon dioxide from a gas-condensate reservoir, through an amine plant and back into a subsurface aquifer. In: Case study: the Sleipner area, Norwegian North Sea. Society of Petroleum Engineers; 2005, p. 96742.

[9] Eiken O, Ringrose P, Hermanrud C, Nazarian B, Torp TA, Høier L. Lessons learned from 14 years of ccs operations: Sleipner, in salah and snøhvit. Energy Procedia 2011;4:5541–8. http://dx.doi.org/10.1016/j.egypro.2011.02.541, URL: https://www.sciencedirect.com/science/article/pii/S1876610211008204. 10th International Conference on Greenhouse Gas Control Technologies.

[10] Baklid A, Korbol R, Owren G. Sleipner vest co2 disposal, co2 injection into a shallow underground aquifer. In: SPE annual technical conference and exhibition. OnePetro; 1996.

[11] Furre AK, Eiken O, Alnes H, Vevatne JN, Kiær AF. 20 Years of monitoring co2-injection at sleipner. Energy Procedia 2017;114:3916–26. http://dx.doi.org/10.1016/j.egypro.2017.03.1523, URL: https://www.sciencedirect.com/science/article/pii/S1876610217317174. 13th International Conference on Greenhouse Gas Control Technologies, GHGT-13, 14-18 2016, Lausanne, Switzerland.

[12] Williams G, Chadwick R. Influence of reservoir-scale heterogeneities on the growth, evolution and migration of a co2 plume at the sleipner field, Norwegian North sea. Int J Greenh Gas Control 2021;106:103260.

[13] Arts R, Chadwick A, Eiken O, Thibeau S, Nooner S. Ten years's experience of monitoring co2 injection in the utsira sand at sleipner, offshore norway. First Break 2008;26. http://dx.doi.org/10.3997/1365-2397.26.1115.27807, URL: https://www.earthdoc.org/content/journals/0.3997/1365-2397.26.1115.27807.

[14] Furre AK, Eiken O. Dual sensor streamer technology used in sleipner co2 injection monitoring. Geophys Prospect 2014;62:1075–88.

[15] Eiken O, Stenvold T, Zumberge M, Alnes H, Sasagawa G. Gravimetric monitoring of gas production from the troll field. Geophysics 2008;73:WA149–54.

[16] Alnes H, Eiken O, Stenvold T. Monitoring gas production and co 2 injection at the sleipner field using time-lapse gravimetry. Geophysics 2008;73:WA155–61.

[17] Alnes H, Eiken O, Nooner S, Sasagawa G, Stenvold T, Zumberge M. Results from sleipner gravity monitoring: Updated density and temperature distribution of the co2 plume. Energy Procedia 2011;4:5504–11. http://dx.doi.org/10.1016/j.egypro.2011.02.536, URL: https://www.sciencedirect.com/science/article/pii/S1876610211008150. 10th International Conference on Greenhouse Gas Control Technologies.

[18] Kang S, Noh K, Seol SJ, Byun J. Mcsem inversion for co2 sequestration monitoring at a deep brine aquifer in a Shallow sea. Explor Geophys 2015;46:236–52.

[19] Salako O, MacBeth C, MacGregor L, Mackay E. Potential applications of time-lapse marine csem to reservoir monitoring. In: 75th EAGE conference & exhibition incorporating SPE EUROPEC 2013. European Association of Geoscientists & Engineers; 2013, p. cp–348.

[20] Chadwick R, Arts R, Eiken O. 4D seismic quantification of a growing co2 plume at sleipner, North sea. In: Geological society, London, petroleum geology conference series. Geological Society of London; 2005, p. 1385–99.

[21] Williams G, Chadwick A. Quantitative seismic analysis of a thin layer of co 2 in the sleipner injection plume. Geophysics 2012;77:R245–56.

[22] Furre AK, Kiær A, Eiken O. Co2-induced seismic time shifts at sleipner. Interpretation 2015;3:SS23–35.

[23] White JC, Williams G, Chadwick A, Furre AK, Kiær A. Sleipner: The ongoing challenge to determine the thickness of a thin co2 layer. Int J Greenh Gas Control 2018;69:81–95. http://dx.doi.org/10.1016/j.ijggc.2017.10.006, URL: https://www.sciencedirect.com/science/article/pii/S1750583617304772.

[24] Chadwick A, Williams G, Delepine N, Clochard V, Labat K, Sturton S, Buddensiek ML, Dillen M, Nickel M, Lima AL, Arts R, Neele F, Rossi G. Quantitative analysis of time-lapse seismic monitoring data at the sleipner co2 storage operation. Lead Edge 2010;29:170–7. http://dx.doi.org/10.1190/1.3304820, arXiv:https://doi.org/10.1190/1.3304820.

[25] Romdhane A, Querendez E. Co2 characterization at the sleipner field with full waveform inversion: Application to synthetic and real data. Energy Procedia 2014;63:4358–65.

[26] Clochard V, Delépine N, Labat K, Ricarte P. Co2 plume imaging using 3d prestack stratigraphic inversion: A case study on the sleipner field. First Break 2010;(28).

[27] Chadwick R, Noy D. History-matching flow simulations and time-lapse seismic data from the sleipner co2 plume. In: Geological society, London, petroleum geology conference series. Geological Society of London; 2010, p. 1171–82.

[28] Cavanagh A. Benchmark calibration and prediction of the sleipner co2 plume from 2006 to 2012. Energy Procedia 2013;37:3529–45. http://dx.doi.org/10.1016/j.egypro.2013.06.246, URL: https://www.sciencedirect.com/science/article/pii/S187661021300489X. gHGT-11 Proceedings of the 11th International Conference on Greenhouse Gas Control Technologies, 18-22 November 2012, Kyoto, Japan.

[29] Cavanagh AJ, Haszeldine RS. The sleipner storage site: Capillary flow modeling of a layered co2 plume requires fractured shale barriers within the utsira formation. Int J Greenh Gas Control 2014;21:101–12. http://dx.doi.org/10.1016/j.ijggc.2013.11.017, URL: https://www.sciencedirect.com/science/article/pii/S1750583613004192.

[30] Zhu C, Zhang G, Lu P, Meng L, Ji X. Benchmark modeling of the sleipner co2 plume: Calibration to seismic data for the uppermost layer and model sensitivity analysis. Int J Greenh Gas Control 2015;43:233–46, URL: https://www.sciencedirect.com/science/article/pii/S1750583614003958.

[31] Williams GA, Chadwick RA. An improved history-match for layer spreading within the sleipner plume including thermal propagation effects. Energy Procedia 2017;114:2856–70. http://dx.doi.org/10.1016/j.egypro.2017.03.1406, URL: https://www.sciencedirect.com/science/article/pii/S1876610217315916. 13th International Conference on Greenhouse Gas Control Technologies, GHGT-13, 14-18 November 2016, Lausanne, Switzerland.

[32] Cui J, Cheng L. A theoretical study of the occurrence state of shale oil based on the pore sizes of mixed Gaussian distribution. Fuel 2017;206:564–71.

[33] Cui J, Sang Q, Li Y, Yin C, Li Y, Dong M. Liquid permeability of organic nanopores in shale: calculation and analysis. Fuel 2017;202:426–34.

[34] Ronneberger O, Fischer P, Brox T. U-net: Convolutional networks for biomedical image segmentation. In: International conference on medical image computing and computer-assisted intervention. Springer; 2015, p. 234–41.

[35] Badrinarayanan V, Kendall A, Cipolla R. Segnet: A deep convolutional encoder–decoder architecture for image segmentation. IEEE Trans Pattern Anal Mach Intell 2017;39:2481–95.

[36] Chen LC, Papandreou G, Kokkinos I, Murphy K, Yuille AL. Deeplab: Semantic image segmentation with deep convolutional nets, atrous convolution, and fully connected crfs. IEEE Trans Pattern Anal Mach Intell 2017;40:834–48.

[37] Girshick R, Donahue J, Darrell T, Malik J. Rich feature hierarchies for accurate object detection and semantic segmentation. In: Proceedings of the IEEE conference on computer vision and pattern recognition. 2014, p. 580–7.

[38] Girshick R. Fast r-cnn. In: Proceedings of the IEEE international conference on computer vision. 2015, p. 1440–8.

[39] Ren S, He K, Girshick R, Sun J. Faster R-CNN: Towards real-time object detection with region proposal networks. In: Advances in neural information processing systems. 2015, p. 91–9.

[40] Redmon J, Divvala S, Girshick R, Farhadi A. You only look once: Unified, real-time object detection. In: Proceedings of the IEEE conference on computer vision and pattern recognition. 2016, p. 779–88.

[41] Dai J, Li Y, He K, Sun J. R-fcn: Object detection via region-based fully convolutional networks. In: Advances in neural information processing systems. 2016, p. 379–87.

[42] He K, Gkioxari G, Dollár R. Mask R-CNN. In: Computer vision (ICCV), 2017 IEEE international conference on. IEEE; 2017, p. 2980–8.

[43] Bolya D, Zhou C, Xiao F, Lee YJ. Yolact: Real-time instance segmentation. In: Proceedings of the IEEE/CVF international conference on computer vision. 2019, p. 9157–66.

[44] Xie E, Sun P, Song X, Wang W, Liu X, Liang D, Shen C, Luo P. Polarmask: Single shot instance segmentation with polar representation. In: Proceedings of the IEEE/CVF conference on computer vision and pattern recognition. 2020, p. 12193–202.

[45] Zhang Y, Lu P, Yu H, Morris S. Enhancement of seismic imaging: An innovative deep learning approach. 2019, arXiv preprint arXiv:1909.06016.

[46] Yang F, Ma J. Deep-learning inversion: A next-generation seismic velocity model building method. Geophysics 2019;84:R583–99. http://dx.doi.org/10.1190/geo2018-0249.1, arXiv:https://doi.org/10.1190/geo2018-0249.1.

[47] Sun A, Scanlon B, Save H, Rateb A. Reconstruction of grace total water storage through automated machine learning. Water Resour Res 2021;(57). http://dx.doi.org/10.1029/2020WR028666.

[48] Kaur H, Zhong Z, Sun A, Fomel S. Time-lapse seismic data inversion for estimating reservoir parameters using deep learning. Interpretation 2021;1–91. http://dx.doi.org/10.1190/int-2020-0205.1.

[49] Di H, Shafiq MA, Wang Z, AlRegib G. Improving seismic fault detection by super-attribute-based classification. Interpretation 2019;7:SE251–67.

[50] Wu X, Liang L, Shi Y, Fomel S. FaultSeg3D: using synthetic datasets to train an end-to-end convolutional neural network for 3D seismic fault segmentation. Geophysics 2019;84:IM35–45.

[51] Di H, Wang Z, AlRegib G. Deep convolutional neural networks for seismic salt-body delineation. In: AAPG annual convention and exhibition. 2018.

[52] Shi Y, Wu X, Fomel S. Saltseg: Automatic 3D salt segmentation using a deep convolutional neural network. Interpretation 2019;7:SE113–22.

[53] Wu X, Yan S, Qi J, Zeng H. Deep learning for characterizing paleokarst collapse features in 3-d seismic images. J Geophys Res: Solid Earth 2020b;125:e2020JB019685.

[54] Geng Z, Wu X, Shi Y, Fomel S. Deep learning for relative geologic time and seismic horizons. Geophysics 2019. in revision.

[55] Wu X, Geng Z, Shi Y, Pham N, Fomel S, Caumon G. Building realistic structure models to train convolutional neural networks for seismic structural interpretation. Geophysics 2020a;85:WA27–39.

[56] Pham N, Fomel S, Dunlap D. Automatic channel detection using deep learning. Interpretation 2019;7:SE43–50.

[57] Gao H, Wu X, Liu G. Channelseg3d: channel simulation and deep learning for channel interpretation in 3d seismic images. Geophysics 2021;86:1–50.

[58] Zhong Z, Sun A, Ren B, Wang Y. A deep-learning-based approach for reservoir production forecast under uncertainty. SPE J 2021;26:1–27. http://dx.doi.org/10.2118/205000-PA.

[59] Zhong Z, Sun A, Qian Y, Ouyang Q. A deep learning approach to anomaly detection in geological carbon sequestration sites using pressure measurements. J Hydrol 2019a;(573). http://dx.doi.org/10.1016/j.jhydrol.2019.04.015.

[60] Zhong Z, Sun AY, Jeong H. Predicting co2 plume migration in heterogeneous formations using conditional deep convolutional generative adversarial network. Water Resour Res 2019b;55:5830–51. http://dx.doi.org/10.1029/2018WR024592, URL: https://agupubs.onlinelibrary.wiley.com/doi/abs/10.1029/2018WR024592. arXiv:https://agupubs.onlinelibrary.wiley.com/doi/pdf/10.1029/2018WR024592.

[61] Liu M, Grana D. Petrophysical characterization of deep saline aquifers for co2 storage using ensemble smoother and deep convolutional autoencoder. Adv Water Resour 2020;142:103634. http://dx.doi.org/10.1016/j.advwatres.2020.103634, URL: https://www.sciencedirect.com/science/article/pii/S0309170819311509.

[62] Wang Z, Dilmore RM, Harbert W. Inferring co2 saturation from synthetic surface seismic and downhole monitoring data using machine learning for leakage detection at co2 sequestration sites. Int J Greenh Gas Control 2020;100:103115. http://dx.doi.org/10.1016/j.ijggc.2020.103115, URL: https://www.sciencedirect.com/science/article/pii/S1750583619304591.

[63] Shokouhi P, Kumar V, Prathipati S, Hosseini SA, Giles CL, Kifer D. Physics-informed deep learning for prediction of co2 storage site response. J Contam Hydrol 2021;241:103835. http://dx.doi.org/10.1016/j.jconhyd.2021.103835, URL: https://www.sciencedirect.com/science/article/pii/S0169772221000747.

[64] Li D, Peng S, Guo Y, Lu Y, Cui X. Co2 storage monitoring based on time-lapse seismic data via deep learning. Int J Greenh Gas Control 2021;108:103336. http://dx.doi.org/10.1016/j.ijggc.2021.103336, URL: https://www.sciencedirect.com/science/article/pii/S1750583621000888.

[65] Li B, Li YE. Neural network-based co2 interpretation from 4d sleipner seismic images. J Geophys Res: Solid Earth 2021;126:e2021JB022524. http://dx.doi.org/10.1029/2021JB022524, URL: https://agupubs.onlinelibrary.wiley.com/doi/abs/10.1029/2021JB022524. arXiv:https://agupubs.onlinelibrary.wiley.com/doi/pdf/10.1029/2021JB022524. e2021JB022524 2021JB022524.

[66] Ringrose P. 2020. Springer.

[67] Chadwick R, Zweigel P, Gregersen U, Kirby G, Holloway S, Johannessen P. Geological reservoir characterization of a co2 storage site: The utsira sand, sleipner, northern North sea. Energy 2004;29:1371–81. http://dx.doi.org/10.1016/j.energy.2004.03.071, URL: https://www.sciencedirect.com/science/article/pii/S0360544204001549. 6th International Conference on Greenhouse Gas Control Technologies.

[68] Singh V, Cavanagh A, Hansen H, Nazarian B, Iding M, Ringrose P. Reservoir modeling of CO2 plume behavior calibrated against monitoring data from sleipner, Norway. 2010, http://dx.doi.org/10.2118/134891-MS, sPE-134891-MS.

[69] Equinor. Sleipner 4d seismic dataset. 2020, http://dx.doi.org/10.11582/2020.00005, Retrieved from https://co2datashare.org/dataset/cbdc354c-fa61-4ab4-a0b4-134e1350a82b.

[70] Cowton L, Neufeld J, White N, Bickle M, Williams G, White J, Chadwick R. Benchmarking of vertically-integrated co2 flow simulations at the sleipner field, North sea. Earth Planet Sci Lett 2018;491:121–33.

[71] Cho Y, Jun H. Estimation and uncertainty analysis of the co2 storage volume in the sleipner field via 4d reversible-jump Markov-chain Monte Carlo. J Pet Sci Eng 2021;200:108333.

[72] Gardner G, Gardner L, Gregory A. Formation velocity and density—the diagnostic basics for stratigraphic traps. Geophysics 1974;39:770–80.

[73] Dupuy B, Ghaderi A, Querendez E, Mezyk M, et al. Constrained avo for co2 storage monitoring at sleipner. Energy Procedia 2017;114:3927–36.

[74] Hale D. Structure-oriented smoothing and semblance. CWP report 635, 2009.

[75] Ghaderi A, Landrø M. Estimation of thickness and velocity changes of injected carbon dioxide layers from prestack time-lapse seismic data. Geophysics 2009;74:O17–28.

[76] Landrø M, Zumberge M. Estimating saturation and density changes caused by co2 injection at sleipner — using time-lapse seismic amplitude-variation-with-offset and time-lapse gravity. Interpretation 2017;5:T243–57. http://dx.doi.org/10.1190/INT-2016-0120.1, arXiv:https://doi.org/10.1190/INT-2016-0120.1.

[77] Kingma DP, Ba J. Adam: A method for stochastic optimization. 2014, CoRR abs/1412.6980. URL: http://dblp.uni-trier.de/db/journals/corr/corr1412.html#KingmaB14.

[78] Lorensen WE, Cline HE. Marching cubes: A high resolution 3D surface construction algorithm. In: ACM SIGGRAPH computer graphics. ACM; 1987, p. 163–9.

[79] Wu X, Fomel S. Least-squares horizons with local slopes and multigrid correlations. Geophysics 2018;83:IM29–40. http://dx.doi.org/10.1190/geo2017-0830.1.

[80] Furre AK, Ringrose P, Santi A. Observing the invisible – co2 feeder chimneys on seismic time-lapse data. 2019, http://dx.doi.org/10.3997/2214-4609.201901646.

[81] Kazemeini SH, Juhlin C, Fomel S. Monitoring co2 response on surface seismic data; a rock physics and seismic modeling feasibility study at the co2 sequestration site, Ketzin, Germany. J Appl Geophys 2010;71:109–24. http://dx.doi.org/10.1016/j.jappgeo.2010.05.004, URL: https://www.sciencedirect.com/science/article/pii/S0926985110000595.

[82] Hale D. Dynamic warping of seismic images. Geophysics 2013;78:S105–15.